


2010-01-01

# Microstructure Investigation Of Al-Rich Titanium Aluminum Alloys

David Pham

*University of Texas at El Paso, [dpham@miners.utep.edu](mailto:dpham@miners.utep.edu)*

Follow this and additional works at: [https://digitalcommons.utep.edu/open\\_etd](https://digitalcommons.utep.edu/open_etd)

 Part of the [Aerospace Engineering Commons](#), [Materials Science and Engineering Commons](#), and the [Mechanics of Materials Commons](#)

---

## Recommended Citation

Pham, David, "Microstructure Investigation Of Al-Rich Titanium Aluminum Alloys" (2010). *Open Access Theses & Dissertations*. 2754.  
[https://digitalcommons.utep.edu/open\\_etd/2754](https://digitalcommons.utep.edu/open_etd/2754)

This is brought to you for free and open access by DigitalCommons@UTEP. It has been accepted for inclusion in Open Access Theses & Dissertations by an authorized administrator of DigitalCommons@UTEP. For more information, please contact [lweber@utep.edu](mailto:lweber@utep.edu).

MICROSTRUCTURE INVESTIGATION OF AL-RICH TITANIUM  
ALUMINUM ALLOYS

DAVID PHAM

Department of Mechanical Engineering

APPROVED:

---

Arturo Bronson, Ph.D., Chair

---

Ahsan R. Choudhuri, Ph.D.

---

Felicia S. Manciu, Ph.D.

---

Patricia D. Witherspoon, Ph.D.  
Dean of the Graduate School

Copyright  
by  
David Pham  
2010

MICROSTRUCTURE INVESTIGATION OF AL-RICH TITANIUM  
ALUMINUM ALLOYS

by

DAVID PHAM

THESIS

Presented to the Faculty of the Graduate School of

The University of Texas at El Paso

in Partial Fulfillment

of the Requirements

for the Degree of

MASTER OF SCIENCE

Department of Mechanical Engineering

THE UNIVERSITY OF TEXAS AT EL PASO

May 2010

## **Acknowledgement**

I would like to extend my deepest gratitude to Dr. Arturo Bronson for guiding me throughout my graduate career and for his advice and support. I would also like to thank Dr. Felicia Manciu for all the advice she had given me that has made the completion of my degree less strenuous and Dr. Ahsan Choudhuri for his support that has made my degree possible.

Lastly, I would also like to thank my friends and family for their ideas and unwavering support during my education.

## **Abstract**

The microstructures of Ti-Al alloys with 70-80 wt% Al were investigated. Aluminum wire (99.999%) and  $\text{TiH}_2$  powder (99.7%) were used to produce the sample compositions inside a vertical tube furnace at  $1600^\circ\text{C}$  in an Ar atmosphere. Argon is purified through a dehumidification and deoxidation system. Magnesium perchlorate  $\text{Mg}(\text{ClO}_4)_2$  acts as a desiccant and titanium sponge pulls oxygen from the Ar in furnaces operating at  $800^\circ\text{C}$  and  $750^\circ\text{C}$ . X-ray diffraction and an optical microscope are used to identify phases and compositions.

## Table of Contents

|  |      |
|--|------|
| Acknowledgement .....                        | iv   |
| Abstract .....                               | v    |
| List of Figures .....                        | viii |
| Chapter 1: Introduction .....                | 1    |
| 1.1 Overview .....                           | 1    |
| 1.2 Objective .....                          | 2    |
| Chapter 2: Literature Review .....           | 3    |
| 2.1 Aluminum Foam .....                      | 3    |
| 2.1.1 Roll-Bonding .....                     | 3    |
| 2.1.2 Melt Stirring .....                    | 3    |
| 2.1.3 Powder Compaction .....                | 4    |
| 2.2 Hydrogen Storage Materials .....         | 5    |
| 2.3 Ti-Al System .....                       | 7    |
| 2.3.1 Ti-Al Phase Diagram .....              | 7    |
| 2.3.2 Ti-Al Microstructure .....             | 9    |
| 2.4 Ti-H System .....                        | 14   |
| 2.4.1 Ti-H Phase Diagram .....               | 14   |
| 2.4.2 TiH <sub>2</sub> Dehydrogenation ..... | 15   |
| 2.5 Ti-Al-H System .....                     | 17   |

|                                      |   |    |
|--------------------------------------|---|----|
| 2.6                                  | Ti-C-O Stability Diagram.....                           | 18 |
| 2.7                                  | Ellingham Diagram for Oxides (Gibb's Free Energy) ..... | 19 |
| Chapter 3: Research Methodology..... |   | 21 |
| 3.1                                  | Sample Preparation and Experimental System .....        | 21 |
| 3.2                                  | Argon Purification System .....                         | 23 |
| 3.3                                  | Experimental Procedure .....                            | 24 |
| Chapter 4: Results .....             |   | 26 |
| Chapter 5: Discussions.....          |   | 46 |
| Chapter 6: Conclusion.....           |   | 50 |
| References.....                      |   | 51 |
| Curriculum Vita.....                 |   | 54 |



## List of Figures

|  |    |
|--|----|
| Figure 1: Stereo micrograph of Al alloy foam using titanium hydride (Yang, Hur and He). .....  | 4  |
| Figure 2: Phase diagram calculated by Zhang. Data point references can be found in (Zhang, Chen and Chang).....  | 8  |
| Figure 3: The Ti-Al binary system according to the thermodynamic description as of 2008 (Witusiewicz, Bondar and Hecht). .....   | 9  |
| Figure 4: Microstructure of the $\text{Ti}_{39}\text{Al}_{61}$ alloy. Presented is a TiAl matrix with precipitates of $\text{TiAl}_2$ (Braun and Ellner). .....  | 10 |
| Figure 5: Microstructure of the $\text{Ti}_{36}\text{Al}_{64}$ alloy. Presented is a TiAl and $\text{TiAl}_2$ (Braun and Ellner) . .....   | 11 |
| Figure 6: Microstructure of the $\text{Ti}_{32.7}\text{Al}_{67.3}$ alloy. Shown is $\text{Ti}_5\text{Al}_{11}$ with $\text{TiAl}_2$ precipitates (Braun and Ellner).....   | 11 |
| Figure 7: Microstructure of $\text{Ti}_{29}\text{Al}_{71}$ with $\text{Ti}_5\text{Al}_{11}$ (gray) with $\text{TiAl}_2$ (light gray) precipitates and $\text{TiAl}_3$ (h) (dark) (Braun and Ellner). .....                   | 12 |
| Figure 8: Microstructure of the $\text{Ti}_{31}\text{Al}_{69}$ alloy. Shown is a eutectoid reaction of $\text{TiAl}_2$ and $\text{TiAl}_3$ (h) (Braun and Ellner). .....   | 12 |
| Figure 9: Microstructure of the $\text{Ti}_{27}\text{Al}_{73}$ alloy. Shown is $\text{Ti}_5\text{Al}_{11}$ (light gray) and $\text{TiAl}_3$ (h) (dark) with $\text{Ti}_5\text{Al}_{11}$ precipitates (Braun and Ellner)..... | 13 |
| Figure 10: Microstructure of the $\text{Ti}_{25}\text{Al}_{75}$ alloy. Shown is $\text{TiAl}_3$ (h) almost completely transformed to $\text{TiAl}_3$ (l) and solid solution of Al(Ti) (white) (Braun and Ellner). .....      | 13 |
| Figure 11: Ti-H phase diagram as calculated by Königsberger (Königsberger, Eriksson and Oates). .....  | 15 |
| Figure 12: TG curves of the $\text{TiH}_2$ powder with heating rates of: (a) $10^\circ\text{C}/\text{min}$ , (b) $15^\circ\text{C}/\text{min}$ ,   |    |

|   |    |
|---|----|
| (c)20°C/min, (d)40°C/min (Liu, He and Feng). .....  | 16 |
| Figure 13: TGA plots for (a)83.3nm, (b)36.1nm, and (c)15.9nm particle sizes of TiH <sub>2</sub> (Bhosle, Baburaj and Miranova). .....   | 17 |
| Figure 14: Effect of hydrogen pressure on the Ti-Al binary system. Calculated at 100°C (Qiu, Opalka and Lovvik). .....  | 18 |
| Figure 15: Stability diagram of titanium and its oxides and carbides with partial pressures of oxygen (P <sub>O2</sub> ) and carbon monoxide (P <sub>CO</sub> ). .....  | 19 |
| Figure 16: Gibbs free energy of formation of oxides for titanium and aluminum. ....   | 20 |
| Figure 17: Simple diagram showing the arrangement of the sample crucibles within the larger alumina crucible.....   | 22 |
| Figure 18: Experiment setup showing an alumina tube within a furnace loaded with the samples. ....  | 23 |
| Figure 19: The flow of argon. a) valve, b) Mg(ClO <sub>4</sub> ) <sub>2</sub> , c) needle valve, d) flow meter, e) furnace at 850°C, f) furnace at 700°C, g) Mg(ClO <sub>4</sub> ) <sub>2</sub> , h) tube furnace ..... | 24 |
| Figure 20: XRD profile for several scans for Ti-70 wt% Al. The dominant black scan is the final characteristic scan. ....   | 27 |
| Figure 21: XRD profile for several scans for Ti-73 wt% Al. The dominant black scan is the final characteristic scan. ....   | 28 |
| Figure 22: XRD profile for several scans for Ti-75 wt% Al (bottom sample). The dominant black scan is the final characteristic scan. ....   | 29 |
| Figure 23: XRD profile for several scans for Ti-75 wt% Al (top sample). The dominant black scan is the final characteristic scan. ....  | 30 |
| Figure 24: XRD profile for several scans for Ti-78 wt% Al (cover). The dominant black scan is   |    |

|   |    |
|---|----|
| the final characteristic scan. ....   | 31 |
| Figure 25: XRD profile for several scans for Ti-78 wt% Al (button). The dominant black scan is the final characteristic scan. ....                  | 32 |
| Figure 26: XRD profile for several scans for Ti- 80 wt% Al. The dominant black scan is the final characteristic scan. ....                          | 33 |
| Figure 27: XRD profile for Ti-70 wt% Al with peak identification. Al, Al <sub>3</sub> Ti, and Ti are detected. ....                                 | 35 |
| Figure 28: XRD profile for Ti-73 wt% Al with peak identification. Al, Al <sub>3</sub> Ti and Ti are detected. ....                                  | 36 |
| Figure 29: XRD profile for Ti-75 wt% Al (Bottom Sample with peak identification. Al, Al <sub>3</sub> Ti, Ti and ZrO <sub>2</sub> are detected. .... | 37 |
| Figure 30: XRD profile for Ti-75 wt% Al (Top Sample) with peak identification. Al, Al <sub>3</sub> Ti, Ti and ZrO <sub>2</sub> are detected. ....   | 38 |
| Figure 31: XRD profile for Ti-78 wt% Al (Cover) with peak identification. Al, Al <sub>3</sub> Ti and Ti are detected. ....                          | 39 |
| Figure 32: XRD profile for Ti-78 wt% Al (button) with peak identification. Al, Al <sub>3</sub> Ti, Ti and ZrO <sub>2</sub> are detected. ....       | 40 |
| Figure 33: XRD profile for Ti-80 wt% Al with peak identification. Al, Al <sub>3</sub> Ti, Ti and ZrO <sub>2</sub> are detected. ....                | 41 |
| Figure 34: Microstructure for titanium aluminide – 70 wt% Al. ....  | 42 |
| Figure 35: Microstructure for titanium aluminide – 73 wt% Al. ....  | 43 |
| Figure 36: Microstructure for titanium aluminide – 75 wt% Al. This composition was located on the bottom layer. ....                                | 43 |

|  |    |
|--|----|
| Figure 37: Microstructure for titanium aluminide – 75 wt% Al. This composition was on the top layer.....                                   | 44 |
| Figure 38: Microstructure for titanium aluminide – 78 wt% Al. This composition was the top layer of the sample. ....                       | 44 |
| Figure 39: Microstructure for titanium aluminide – 78 wt% Al. This composition was the button that lay on the bottom of the crucible. .... | 45 |
| Figure 40: Microstructure for titanium aluminide – 80 wt% Al. ....   | 45 |
| Figure 41: Ti-Al-O <sub>2</sub> stability diagram calculated by FactSage at 1123K. ....  | 47 |
| Figure 42: Ti-Al-O <sub>2</sub> stability diagram calculated by FactSage at 973K. ....   | 48 |
| Figure 43: Ti-Al-O <sub>2</sub> stability diagram calculated by FactSage at 1873K. ....  | 48 |
| Figure 44: Ti-H-O stability diagram calculated by FactSage at 1873K.....   | 49 |

## Chapter 1: Introduction

### 1.1 Overview

In a study of Al hydrides, Li et al. determined that an Al hydride ion (i.e.,  $\text{Al}_4\text{H}_6^-$ ) forms from a pulsed arc discharge of an aluminum electrode in a hydrogen gas (Li, Grubisic and Stokes). If the hydride ion could be stabilized sufficiently into a condensed phase, it may be a viable propellant similar to  $\text{AlH}_3$ . The  $\text{AlH}_3$  reacts exothermically with oxygen to create sufficient energy for use as a propellant as Bazyn et al. has reported (Bazyn, Eyer and Krier). When studying the Al hydride formation by reacting Al with  $\text{TiH}_2$ , it was found that the Al-H system and the aluminum rich Ti-Al system have been scarcely investigated. Consequently, the latter system was pursued first to understand the Al-Ti-H system to more effectively find a metastable Al hydride.

The Ti-Al intermetallic system has been considered as a replacement material for the Ni-based superalloys used currently for aerospace applications. The Ti-based alloys have a lower density than the Ni superalloys, but oxidation problems and low ductility at room temperature have prevented their implementation. Furthermore, discrepancies within the Ti-Al binary system have scientists reexamining the phase diagram. The equilibrium temperatures and the phase relations obtained from several investigators do not align properly and thus several interpretations of the phase diagram exist (Braun and Ellner). The Al-rich portion of the phase diagram, especially, has been plagued with ambiguous results that mostly develop from oxygen contamination during experimentation.

The pairing of Ti and Al is also unique unto itself in the way that a reaction between titanium hydride ( $\text{TiH}_2$ ) and liquid Al can create a metallic foam as the hydrogen is released into an Al melt. The subsequent Al-Ti melt forms with sufficient viscosity and low surface tension

enabling a porous structure to stabilize as the liquid solidifies. For a more extensive review of the processing of metallic foams, the reader is referred to Banhart (Banhart). Aluminum foam is an ultra-lightweight alloy with a high stiffness that is extremely capable of absorbing high impact energy. The porosity gives the alloy high impact absorption efficiency and tremendous compressive strength making it ideal for automobile bumpers and crash boxes (Youn and Kang).

Titanium also seems to be a key catalyst into developing hydrogen storage materials that contain a high metal to hydrogen ratio. Complex hydrides such as  $\text{LiAlH}_4$ ,  $\text{NaAlH}_4$ , and  $\text{Na}_3\text{AlH}_6$  were appealing storage materials; however, their inability to reabsorb hydrogen and the difficulty in producing these materials has led the investigation to a different direction. Metal hydrides have been the new front for over 40 years, but their stability impedes the kinetics of dehydrogenation and hydrogenation needed for storage capacity. (Maeland, Hauback and Fjellvag). Metal hydrides require high temperatures to recover hydrogen. Doping metal aluminum hydrides with Ti or  $\text{TiAl}_3$  has the potential effect of activating or catalyzing the hydride surface facilitating hydrogen storage (Maeland, Hauback and Fjellvag).

## **1.2 Objective**

The objective of this research was to investigate the less studied Al-rich portion of the Ti-Al binary system. The solid state reactions with their accompanied thermodynamic relationship will aid in determining the evolution of the phase equilibria.

## **Chapter 2: Literature Review**

Although the core of the study is the aluminum rich side of the Ti-Al system, this section reviews the thermodynamic stability of the Ti-Al-O-H system needed for the synthesis of aluminates and processing of Al foams. The background of the thermodynamic stability of Ti aluminides developed for improving their oxidation can be used to understand the Ti-Al-O-H system.

### **2.1 Aluminum Foam**

Metal foam is a material where a gas has been trapped within a metal matrix creating a highly porous metal. The resulting metal is perforated resulting in a very low density. Most metal foams contain good mechanical properties that respond well to impact energy absorption that lend well to the automotive industry, specifically aluminum foam. Methods used to make Al foams include powder compact melting, melt stirring or melt foaming and roll bonding (Youn and Kang, Yang, Hur, and He, Kitazono, Sato, and Kuribayashi)

#### **2.1.1 Roll-Bonding**

The roll bonding method has been proposed as a new method to fabricate Al foam. An Al plate is cut into two equal pieces and  $\text{TiH}_2$  is sandwiched between the two layers. The plates are then roll bonded and without extra addition of  $\text{TiH}_2$ , the plates are again cut into two equal pieces and rolled. The process is repeated to distribute the  $\text{TiH}_2$  throughout the aluminum matrix and finally heat treated to foam the metal (Kitazono, Sato and Kuribayashi).

#### **2.1.2 Melt Stirring**

In melt stirring, the process can be described with the following steps: melting, thickening, stirring, holding and cooling. Aluminum is first melted within a crucible and a

thickening agent is added to increase the viscosity of the melt. Once the correct viscosity is attained,  $\text{TiH}_2$  powder is dispersed into the melt and stirred. The solution is held at a desired temperature to allow further dehydrogenation of the hydride and finally the crucible is allowed to cool (Yang, Hur and He). The holding temperature should be set to prevent instant combustion of  $\text{TiH}_2$ . If a prolonged stirring time is given, the resulting pores are smaller and distributed throughout the melt. The effects of holding the melt at a certain temperature have plateau effects where after 120 seconds, the porosity characteristics do not change. Yang et al. also took micrographs of the resulting pore structure and can be seen in Figure 1.

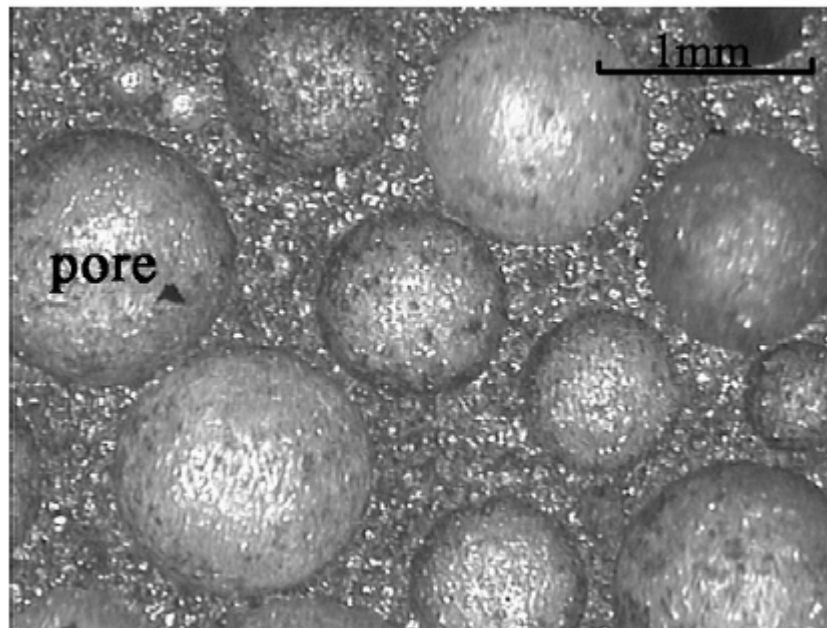


*Figure 1: Stereo micrograph of Al alloy foam using titanium hydride (Yang, Hur and He).*

### **2.1.3 Powder Compaction**

To form Al foam using the powder compact melting process, a precursor must first be made. In powder compact melting, the precursor is crucial to the successful foaming of the metal. The precursor consists of Al powder and a certain percentage of  $\text{TiH}_2$  that has been mixed to homogeneity followed by a heat treatment of the powder at a temperature determined by the



thermal decomposition of the foaming agent ( $\text{TiH}_2$ ) that activates foam formation. The powder is finally compressed before the final heat treatment process at higher temperature, around the melting temperature of Al, where foam formation occurs (Duarte and Banhart).

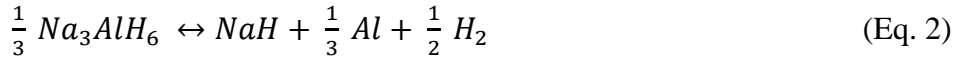
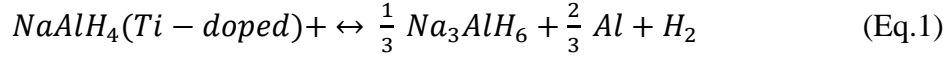
A compacting pressure for complete densification of the precursor is necessary to minimize any porosity to prevent the escape of hydrogen from the metal matrix. A higher densification results in a uniform pore distribution and pore density (Duarte and Banhart).  $\text{TiH}_2$  content and the final heating temperature are also key control variables for a good quality metal foam. Youn and Kang modified the  $\text{TiH}_2$  content and the final heating temperature and compared the foams by analyzing the pore size, pore quantity, and pore distribution. Samples containing 1.0 and 1.5 wt%  $\text{TiH}_2$  displayed the most height increase and round pores while lower concentrations of  $\text{TiH}_2$  showed cracking and elongated pores. Samples with 1.5 wt%  $\text{TiH}_2$  at different final heating temperatures exhibited large and unstable pore growth, and the pores would collapse at temperatures above  $640^\circ\text{C}$ . However, samples with 0.3 wt%  $\text{TiH}_2$  heated to  $680^\circ\text{C}$  showed similar pore growth and pore distribution as a 1.5 wt% sample heated to  $640^\circ\text{C}$  (Youn and Kang).

## **2.2 Hydrogen Storage Materials**

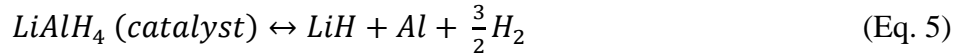
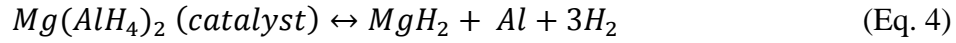
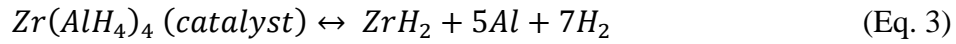
Although there already exist several hydrogen storage materials, none have met the requirements for vehicular application. The problems facing hydrogen storage materials lays in finding a material with a high hydrogen content, sufficient dehydrogenation kinetics, efficient rehydrogenation rates, and a low cost of production (Jensen, Orimo and Nakamori). Investigators have returned to studying hydrogen storage materials when sodium alantes doped with Ti appeared to be a prospective reversible hydrogen storage material, and it has been hypothesized

that a titanium aluminide or titanium hydride may be the catalyst (Maeland, Hauback and Fjellvag).

The following reaction equations are proposed:



And it is predicted that similar results should be seen from other alanates:



NaAlH<sub>4</sub> not doped with Ti released 3.7 wt% H<sub>2</sub> at 210-220°C in 3 hrs; rehydrogenation requires a pressure of 17.5 MPa H<sub>2</sub> at a temperature of 270°C for 2-3 hrs (Orimo, Nakamori and Eliseo). Sun performed cyclic dehydrogenation/rehydrogenation tests on NaAlH<sub>4</sub> doped with Ti and has reported a maximum availability of 3.6 wt% H<sub>2</sub> at 160°C for 3 hr (Sun, Srinivasan and Chen). The available H<sub>2</sub> decreased to 3.0 wt% after 100-12 hour cycles and showed no further reduction of H<sub>2</sub> with a dehydrogenation cycle at 120°C and a pressure of 12 MPa H<sub>2</sub> for 12 hrs. It can be seen that Ti as a catalyst aids in lowering the temperature necessary to liberate H<sub>2</sub> from the alanate and reduces the required H<sub>2</sub> pressure. An agreement with Ti being a catalyst has also been verified by a thermodynamic model of the Al-Na-Ti-H system. Titanium doping encourages the formation of TiH<sub>2</sub> and TiAl<sub>3</sub> which appear to enhance catalytically the hydrogenation/dehydrogenation overall reaction of sodium alanates (Qiu, Opalka and Lovvik). However, the required H<sub>2</sub> pressure is still considered to be too high for practical use for automotive applications (Graetz and Reilly).

## 2.3 Ti-Al System

### 2.3.1 Ti-Al Phase Diagram

The calculated phase diagram proposed by Zhang et al. (1999) accurately depicts the phase relations and equilibrium temperatures acquired experimentally as shown in Figure 2. The Al-rich portion of the phase diagram, has met with uncertainty as several experiments have had trouble with oxygen contamination, skewing the results that have evolved into several regions of the Ti-Al phase diagram. Witusiewicz et al.(2008) made his own thermodynamic model that encompasses a total of 12 phases:  $\alpha$ -Ti (hexagonal close packed – hcp),  $\beta$ -Ti (body centered cubic – bcc),  $\beta_o$  (solid solution  $\beta$ TiAl),  $\alpha_2$ -Ti<sub>3</sub>Al,  $\gamma$ -TiAl, Ti<sub>3</sub>Al<sub>5</sub>,  $\eta$ -TiAl<sub>2</sub>,  $\zeta$ -Ti<sub>2</sub>Al<sub>5</sub>,  $\epsilon(l)$ -TiAl<sub>3</sub>(l),  $\epsilon(h)$ -TiAl<sub>3</sub>(h),  $\alpha$ -Al, and liquid (L). This phase diagram is presented in Figure 3 and will be used as the reference diagram as it matches closely with experimental data and the partial phase diagram presented by Braun (Braun and Ellner). Figure 2 and Figure 3 have highlighted regions marking the 70-80 wt% Al range.

However, not visible in the phase diagram is the existence of face centered cubic titanium. Face centered cubic titanium was first reported in 1969 and Van Heerden et al. formed fcc Ti layers through vapor deposition (Heerden, Josell and Shechtman). Zhang and Ying have discovered fcc titanium through the milling and heating of Al and Ti powders (Zhang and Ying). Heavily milled Ti and Al powders show some transformation of hcp-Ti to fcc-Ti in thin layers. Heating a milled mixture of Al and Ti to 321 °C also displays the transformation process with Al-25 at% Ti and Ti-25 at% Al.

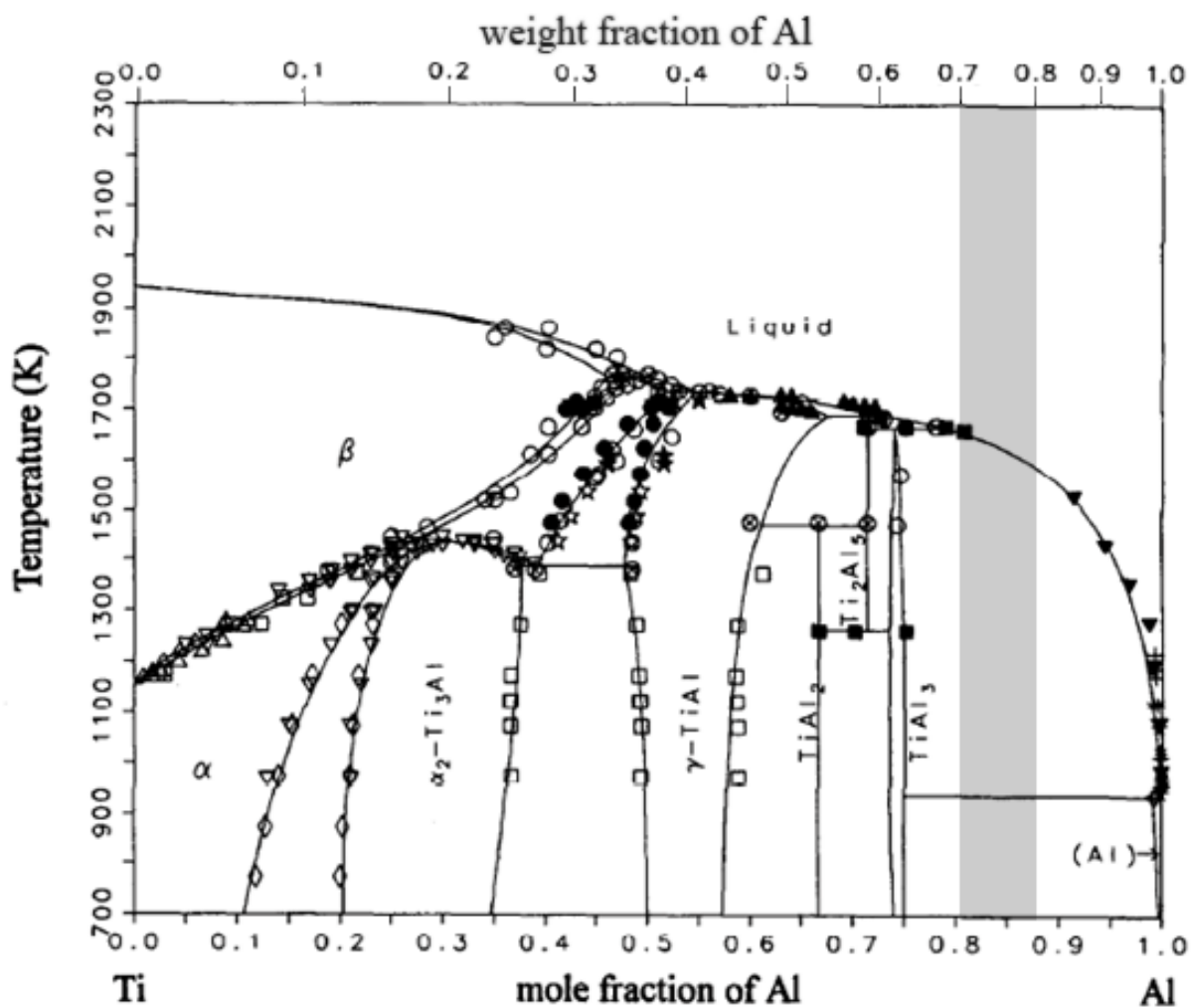


Figure 2: Phase diagram calculated by Zhang. Data point references can be found in (Zhang, Chen and Chang).

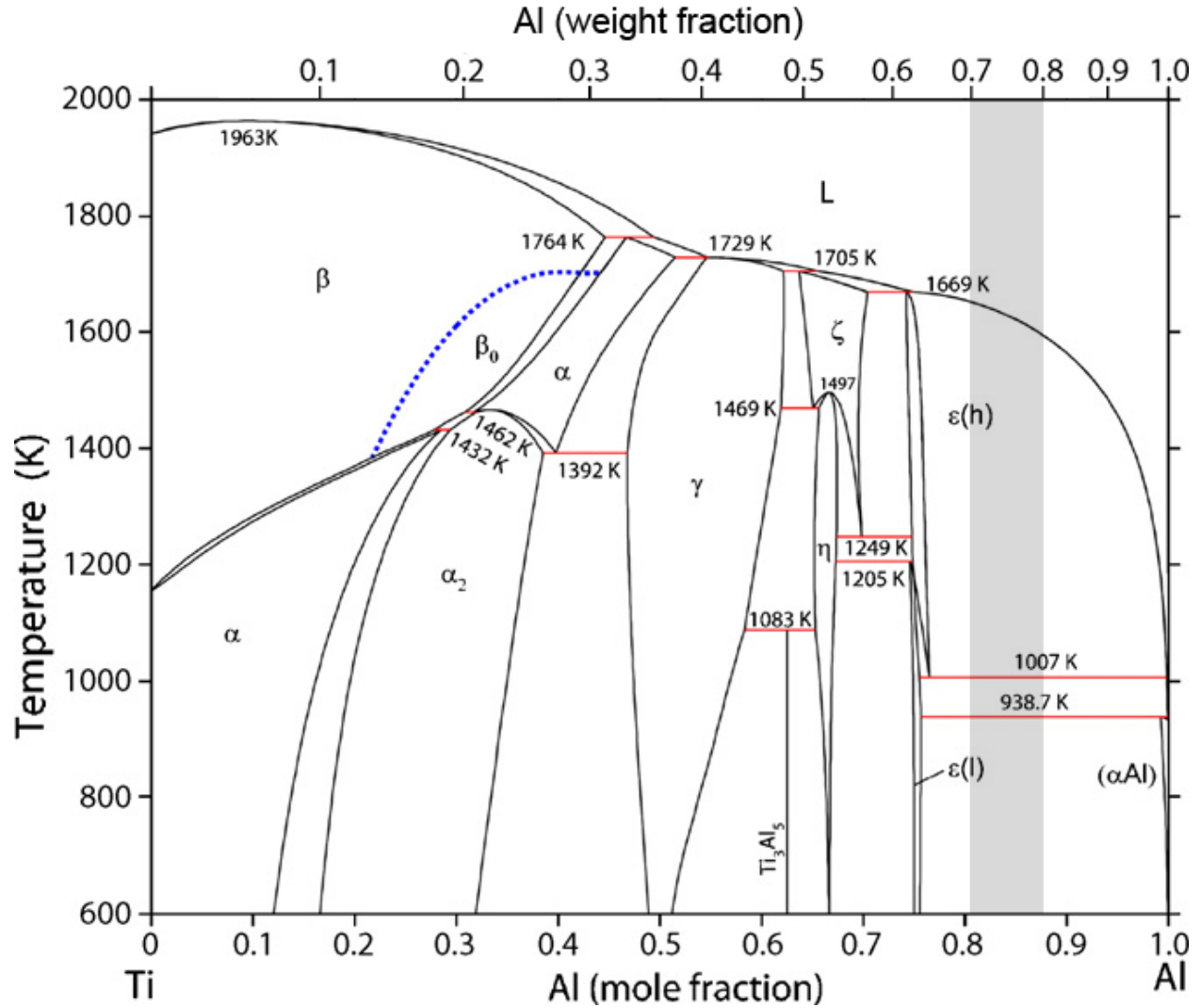
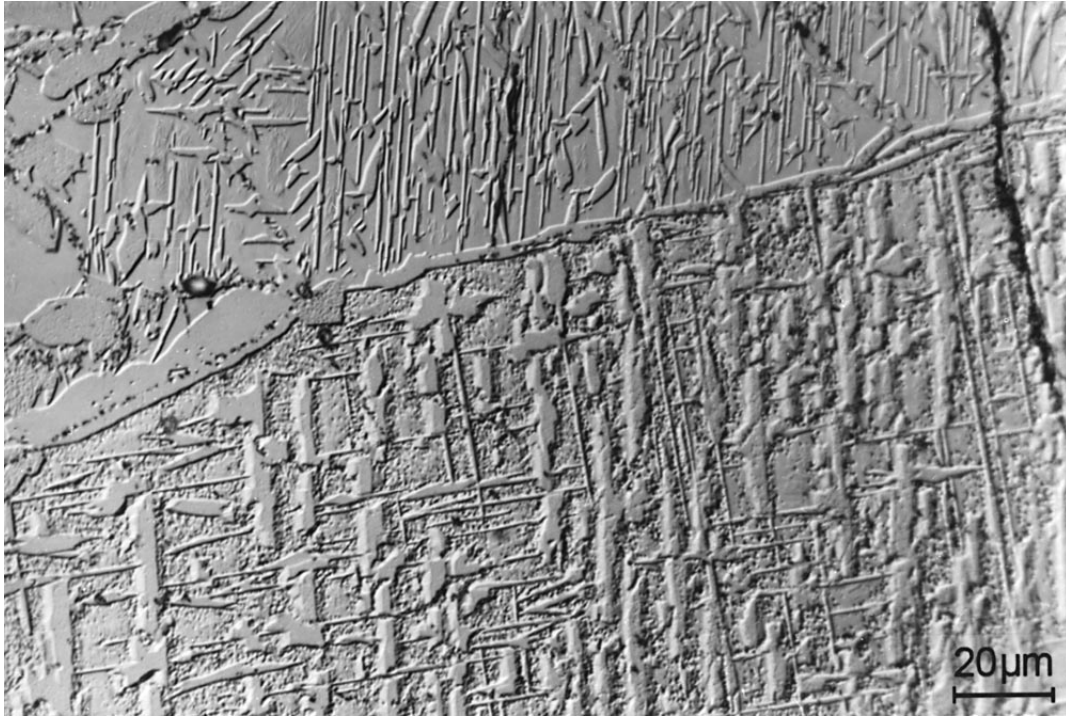


Figure 3: The Ti-Al binary system according to the thermodynamic description as of 2008 (Witusiewicz, Bondar and Hecht).

### 2.3.2 Ti-Al Microstructure

Braun and Ellner thoroughly investigated the Ti-Al system in the range of 50 to 80 at. %Al (Braun and Ellner) with metallographic samples examined with a scanning electron microscope (SEM) using back-scatter electrons (BSE). Figures 4-10 are provided as references to match microstructure characteristics. Samples in the composition range 70 to 74.75 at. % Al

contained the phases  $\text{Ti}_5\text{Al}_{11}$ ,  $\text{TiAl}_3$  (h), and  $\text{Al}(\text{Ti})$ . Samples in the composition range 75 to 80 at. %Al contained  $\text{TiAl}_3$  (h),  $\text{TiAl}_3$  (l) and  $\text{Al}(\text{Ti})$ .  $\text{TiAl}_3$  (h) is a high temperature phase that is seen above  $950^\circ\text{C}$ ,  $\text{TiAl}_3$  (l) is a low temperature phase, and  $\text{Al}(\text{Ti})$  is a solid solution phase.



*Figure 4: Microstructure of the  $\text{Ti}_{39}\text{Al}_{61}$  alloy. Presented is a  $\text{TiAl}$  matrix with precipitates of  $\text{TiAl}_2$  (Braun and Ellner).*

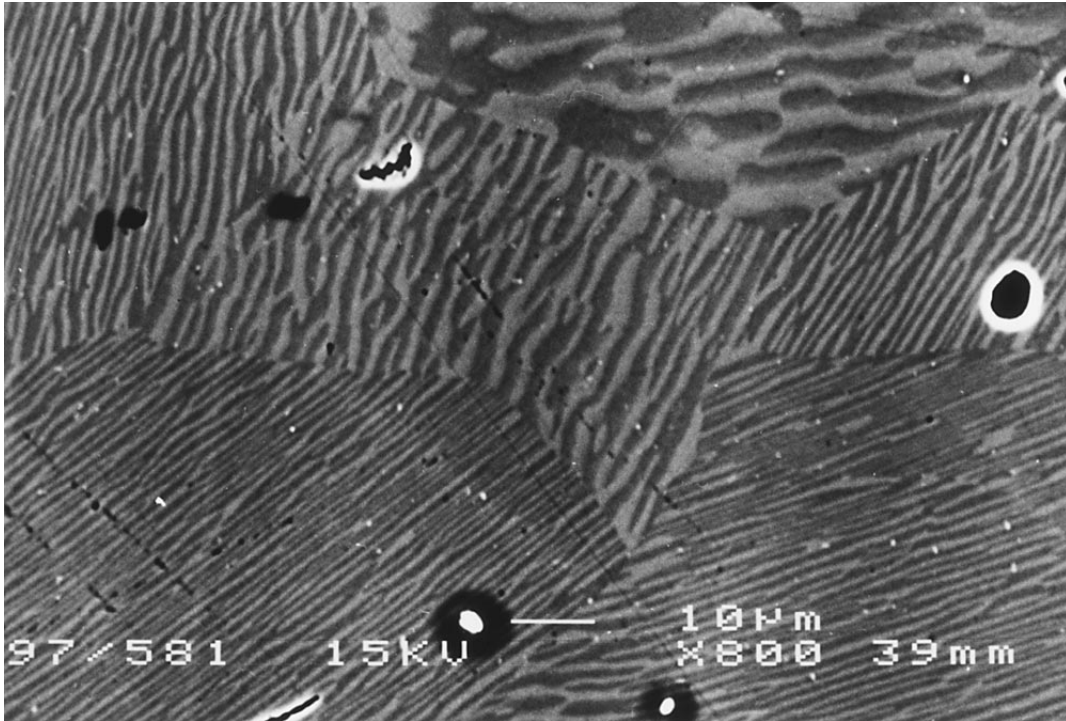


Figure 5: Microstructure of the  $\text{Ti}_{36}\text{Al}_{64}$  alloy. Presented is a  $\text{TiAl}$  and  $\text{TiAl}_2$  (Braun and Ellner).

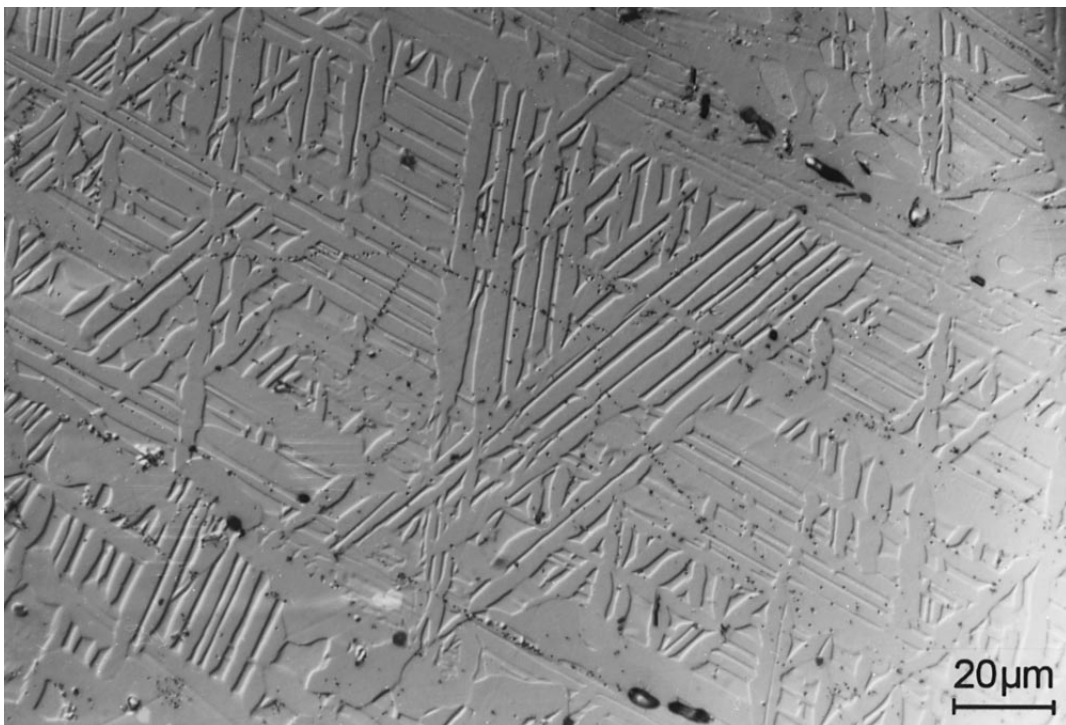


Figure 6: Microstructure of the  $\text{Ti}_{32.7}\text{Al}_{67.3}$  alloy. Shown is  $\text{Ti}_5\text{Al}_{11}$  with  $\text{TiAl}_2$  precipitates (Braun and Ellner).

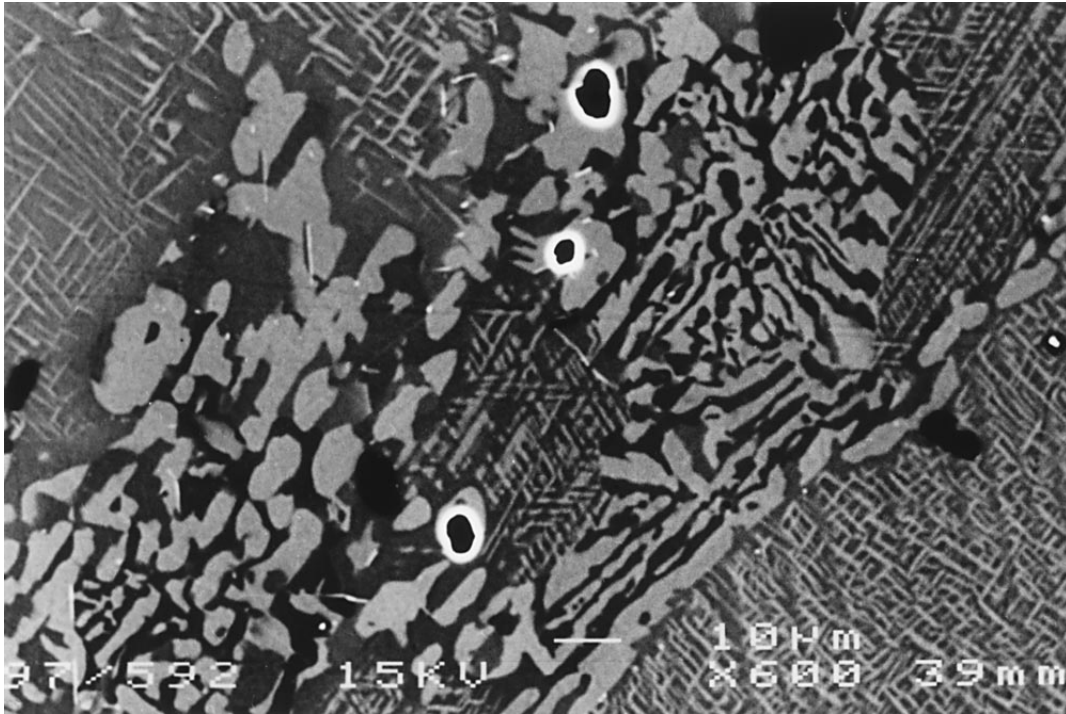


Figure 7: Microstructure of Ti<sub>29</sub>Al<sub>71</sub> with Ti<sub>5</sub>Al<sub>11</sub> (gray) with TiAl<sub>2</sub> (light gray) precipitates and TiAl<sub>3</sub> (h) (dark) (Braun and Ellner).

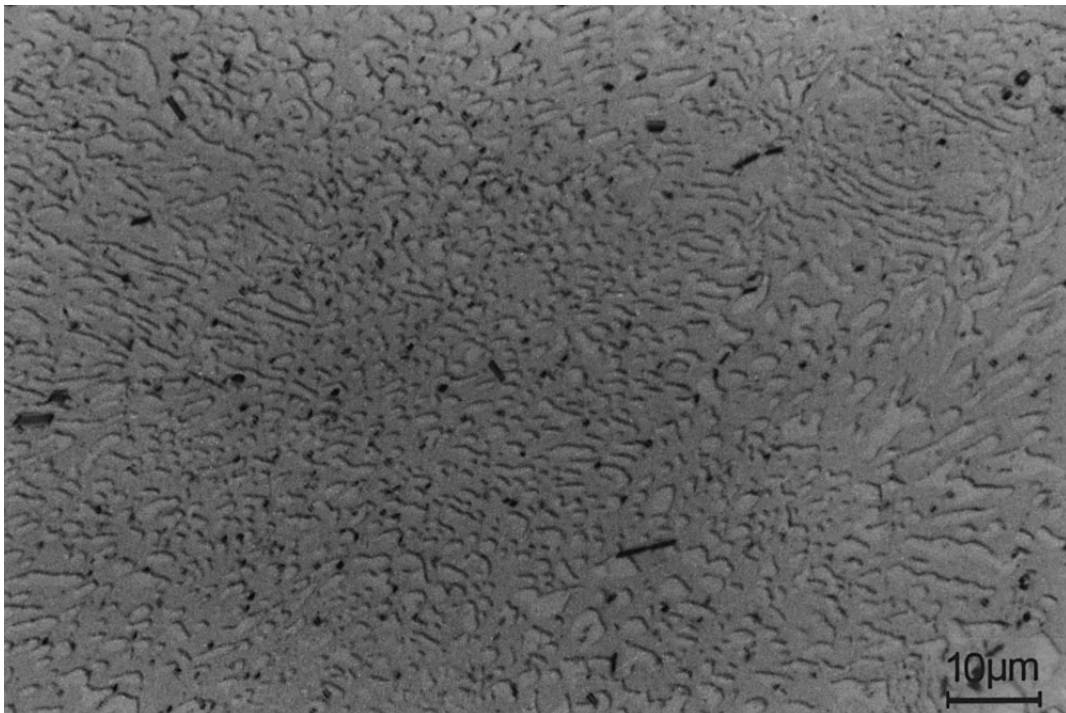


Figure 8: Microstructure of the Ti<sub>31</sub>Al<sub>69</sub> alloy. Shown is a eutectoid reaction of TiAl<sub>2</sub> and TiAl<sub>3</sub>(h) (Braun and Ellner).



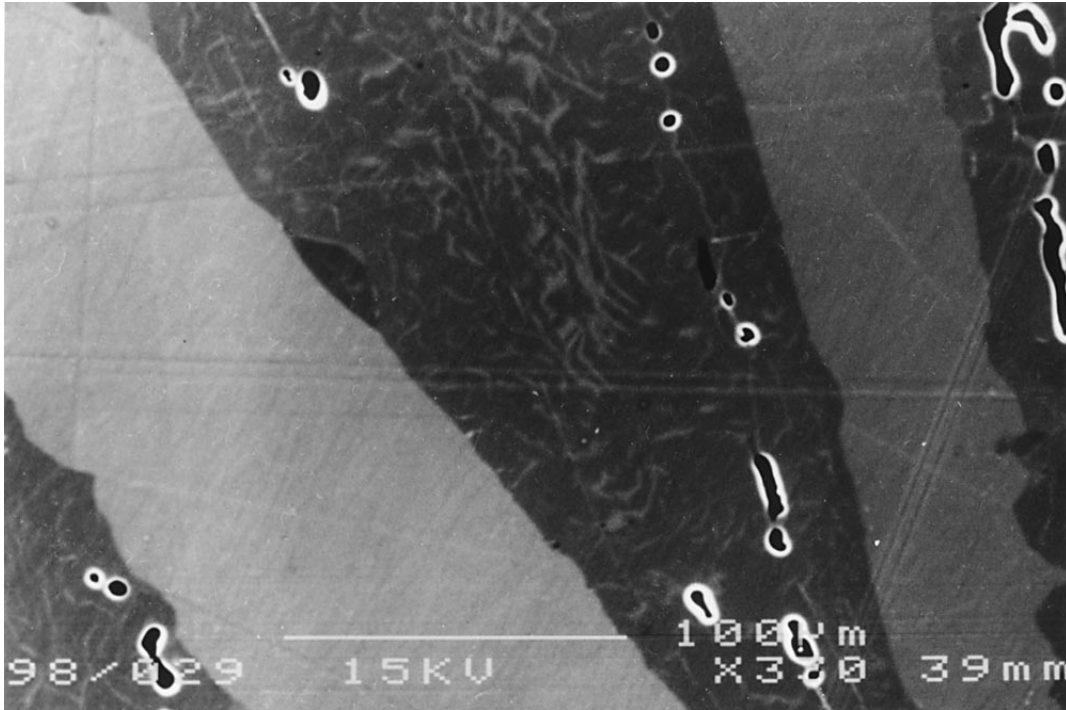


Figure 9: Microstructure of the Ti<sub>27</sub>Al<sub>73</sub> alloy. Shown is Ti<sub>5</sub>Al<sub>11</sub> (light gray) and TiAl<sub>3</sub>(h) (dark) with Ti<sub>5</sub>Al<sub>11</sub> precipitates (Braun and Ellner).

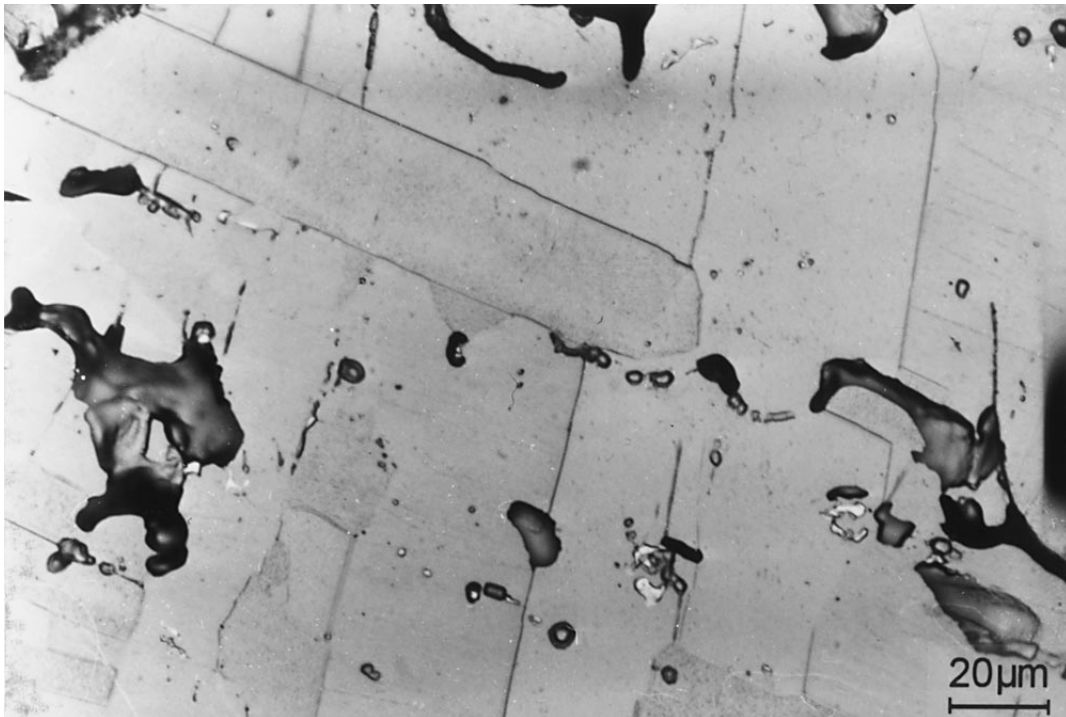


Figure 10: Microstructure of the Ti<sub>25</sub>Al<sub>75</sub> alloy. Shown is TiAl<sub>3</sub>(h) almost completely transformed to TiAl<sub>3</sub>(l) and solid solution of Al(Ti) (white) (Braun and Ellner).

## 2.4 Ti-H System

### 2.4.1 Ti-H Phase Diagram

Previous significant work on the Ti-H system has been done by San-Martin and Manchester in 1987 (San-Martin and Manchester). A revision to their calculated phase diagram came several years later by Wang in 1996 with hydrogen isobars superimposed on the phase diagram, but large uncertainties rendered a misalignment in the bars (Wang).

The most recent has been published by Königsberger (2000) which can be seen in Figure 11 (Königsberger, Eriksson and Oates). The diagram consists of the following phases:  $\alpha$ -Ti (hcp),  $\beta$ -Ti (bcc), and  $\delta$ -TiH<sub>2</sub> (face center cubic hydride). The regions where the pressure isobars are horizontal indicate a two-phase region. A eutectoid reaction at a 41.5 at% H demonstrates a decomposition of the  $\beta$ -phase to the  $\alpha$  and  $\delta$  phases.

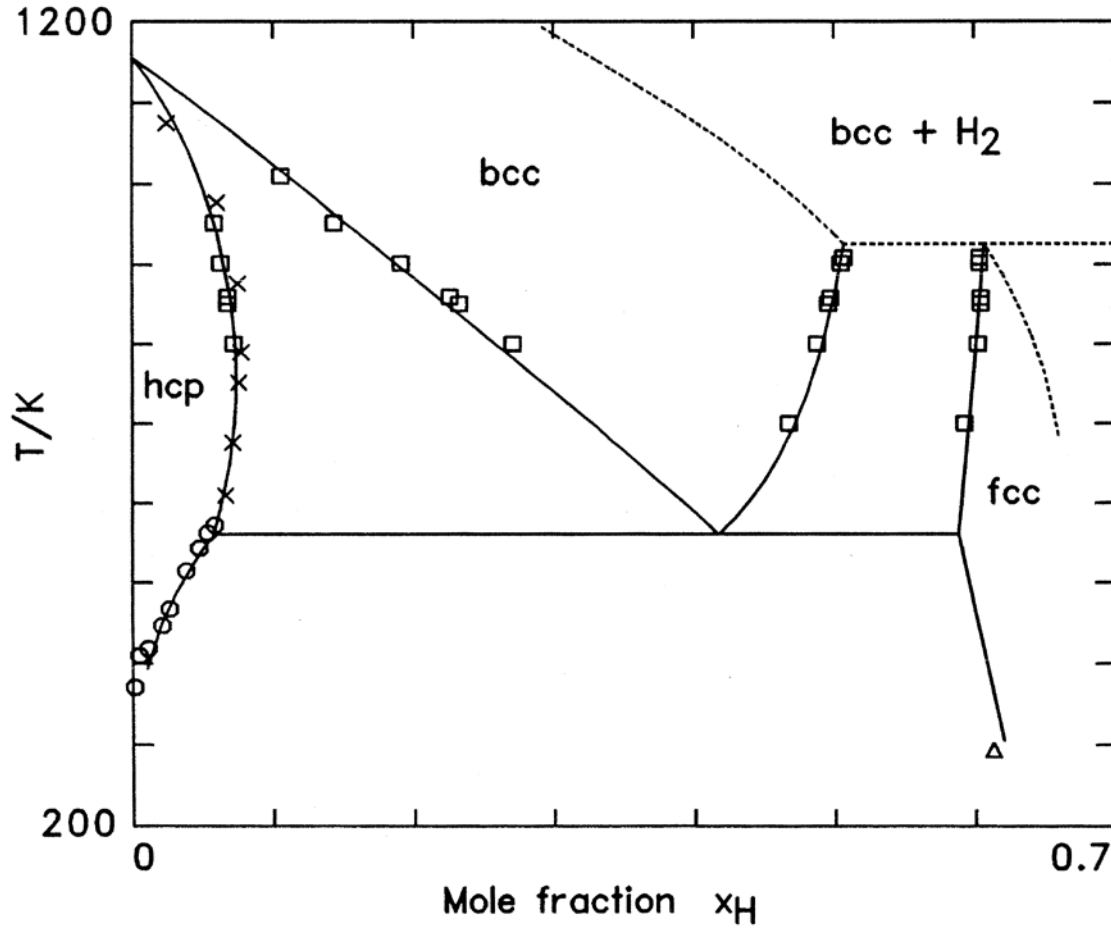


Figure 11: Ti-H phase diagram as calculated by Königsberger (Königsberger, Eriksson and Oates).

#### 2.4.2 TiH<sub>2</sub> Dehydrogenation

The kinetic study of the dehydrogenation of TiH<sub>2</sub> powders have been carried out by Liu. Using TiH<sub>2</sub> powder 50  $\mu\text{m}$  in size, Liu determined the rate at which the hydrogen evolves from the powder at various furnace temperature ramp rates. At ramp rates of 10°C/min, 15°C/min, 20°C/min and 40°C/min the hydrogen begins to liberate at 470°C, 500°C, 515°C and 520°C, respectively. The results can be seen in Figure 12; the results are modified to only show the thermogravimetry curves (Liu, He and Feng).

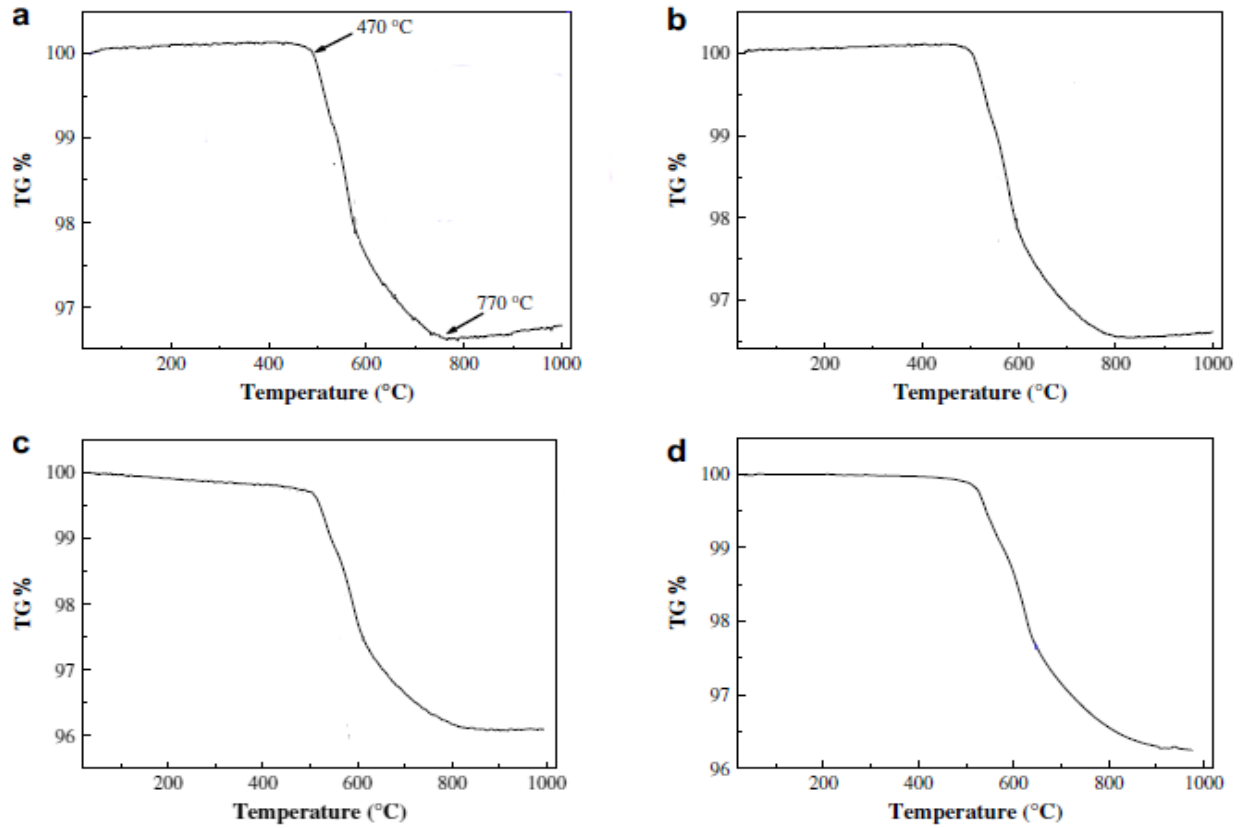


Figure 12: TG curves of the  $\text{TiH}_2$  powder with heating rates of: (a)  $10^\circ\text{C/min}$ , (b)  $15^\circ\text{C/min}$ , (c)  $20^\circ\text{C/min}$ , (d)  $40^\circ\text{C/min}$  (Liu, He and Feng).

Bhosle et al. investigated how the  $\text{TiH}_2$  particle size affects dehydrogenation (Bhosle, Baburaj and Miranova). The results of this investigation can be seen in Figure 13 through thermal gravimetric analysis (TGA). The smaller the  $\text{TiH}_2$  particle size, the faster it releases hydrogen. Although Bhosle et al. was unable to provide a heating rate it can be assumed that the  $\text{TiH}_2$  will be fully dehydrogenated at  $1000^\circ\text{C}$ .

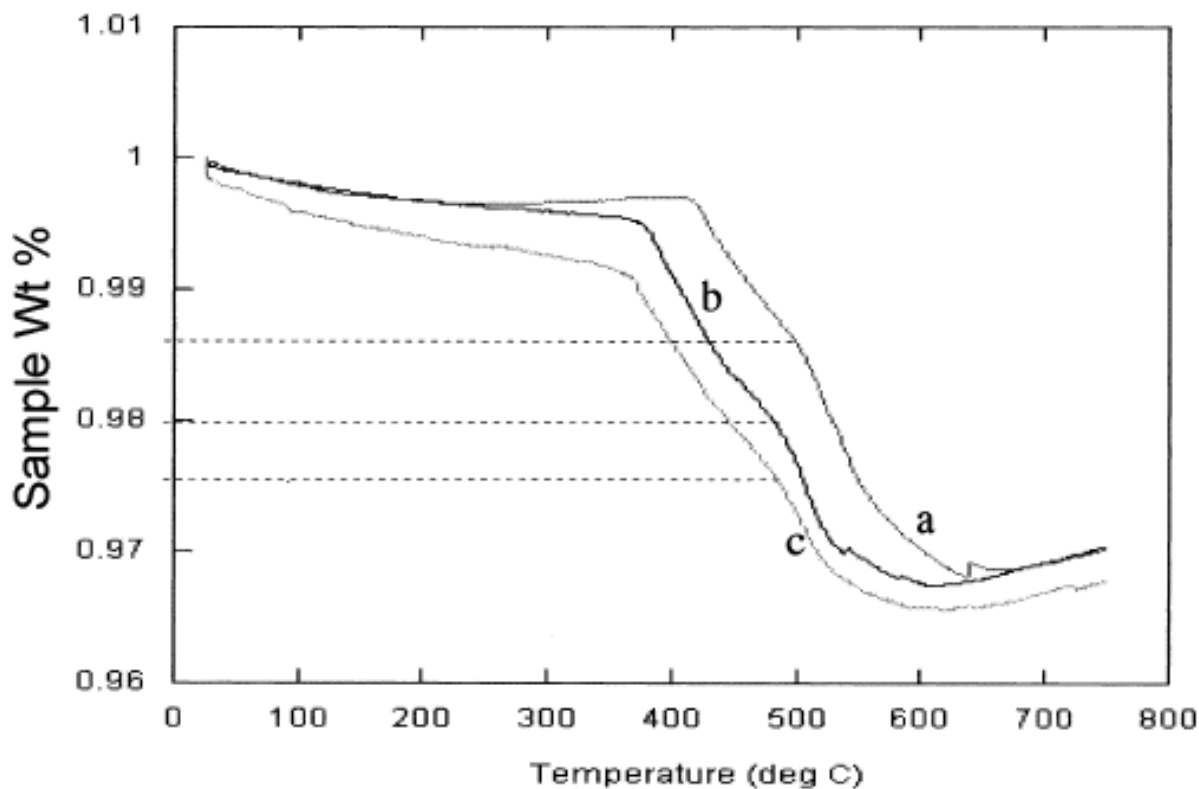


Figure 13: TGA plots for (a)83.3nm, (b)36.1nm, and (c)15.9nm particle sizes of  $\text{TiH}_2$  (Bhosle, Baburaj and Miranova).

## 2.5 Ti-Al-H System

No known ternary compounds exist in the Ti-Al-H system and probably because hydrogen dissolves significantly in  $\alpha$ -Ti (hcp) and  $\beta$ -Ti (bcc) (Qiu, Opalka and Lovvik). There also appears to be large solubility of hydrogen in  $\text{Ti}_3\text{Al}$ .  $\text{Ti}_3\text{Al}$  becomes  $\alpha\text{-Ti}_x\text{Al}_{1-x}\text{H}_y$ , considered to be amorphous, after exposure to a hydrogen atmosphere and reduces back to its original crystal structure. Increasing the content of Al in  $\text{Ti}_3\text{Al}$  decreases the hydrogen solubility and there is no solubility of hydrogen in any other titanium aluminide (Hashi, Ishikawa and Suzuki).

Qiu et al. has calculated the stability of titanium aluminides with respect to hydrogen pressure at 1000°C. The diagram can be seen in Figure 14. Of all the Ti-Al compounds, only  $\text{TiAl}_3$  and  $\text{TiAl}_2$  are stable. However,  $\text{TiAl}_2$  becomes unstable above a hydrogen pressure of  $10^{-3}$

bar.  $\text{TiAl}_3$  remains stable at high hydrogen pressures, a concession to its high solubility of hydrogen (Qiu, Opalka and Lovvik).

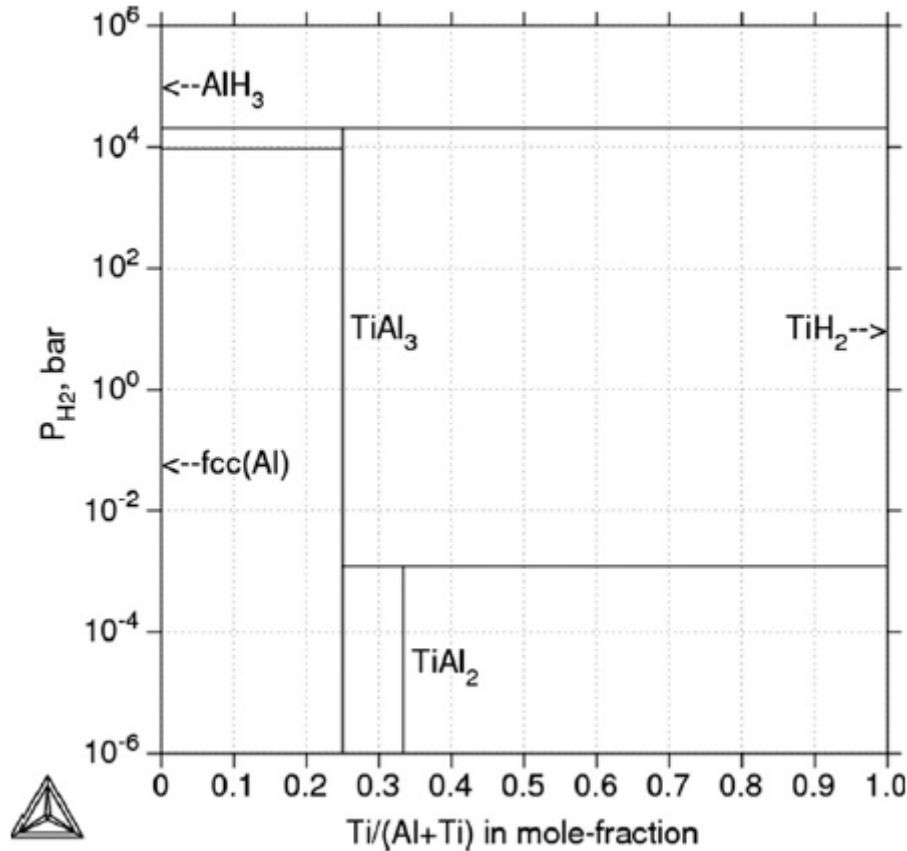


Figure 14: Effect of hydrogen pressure on the Ti-Al binary system. Calculated at  $100^\circ\text{C}$  (Qiu, Opalka and Lovvik).

## 2.6 Ti-C-O Stability Diagram

The stability diagram is an indicator of what species will exist in different atmospheres. Figure 15 is a stability diagram calculated at  $1600^\circ\text{C}$  with CO and  $\text{O}_2$  using the FactSage software package (Version 6.1). The first oxide to form will be TiO having an oxygen partial pressure ( $P_{\text{O}_2}$ ) stability range approximately between -20.5 and -15.5 atm. If more oxygen is introduced into the system, TiO will convert into  $\text{Ti}_2\text{O}_3$ ,  $\text{Ti}_3\text{O}_5$  and onto the magnelli phases of  $\text{Ti}_x\text{O}_{2x-1}$  and finally to  $\text{TiO}_2$ .

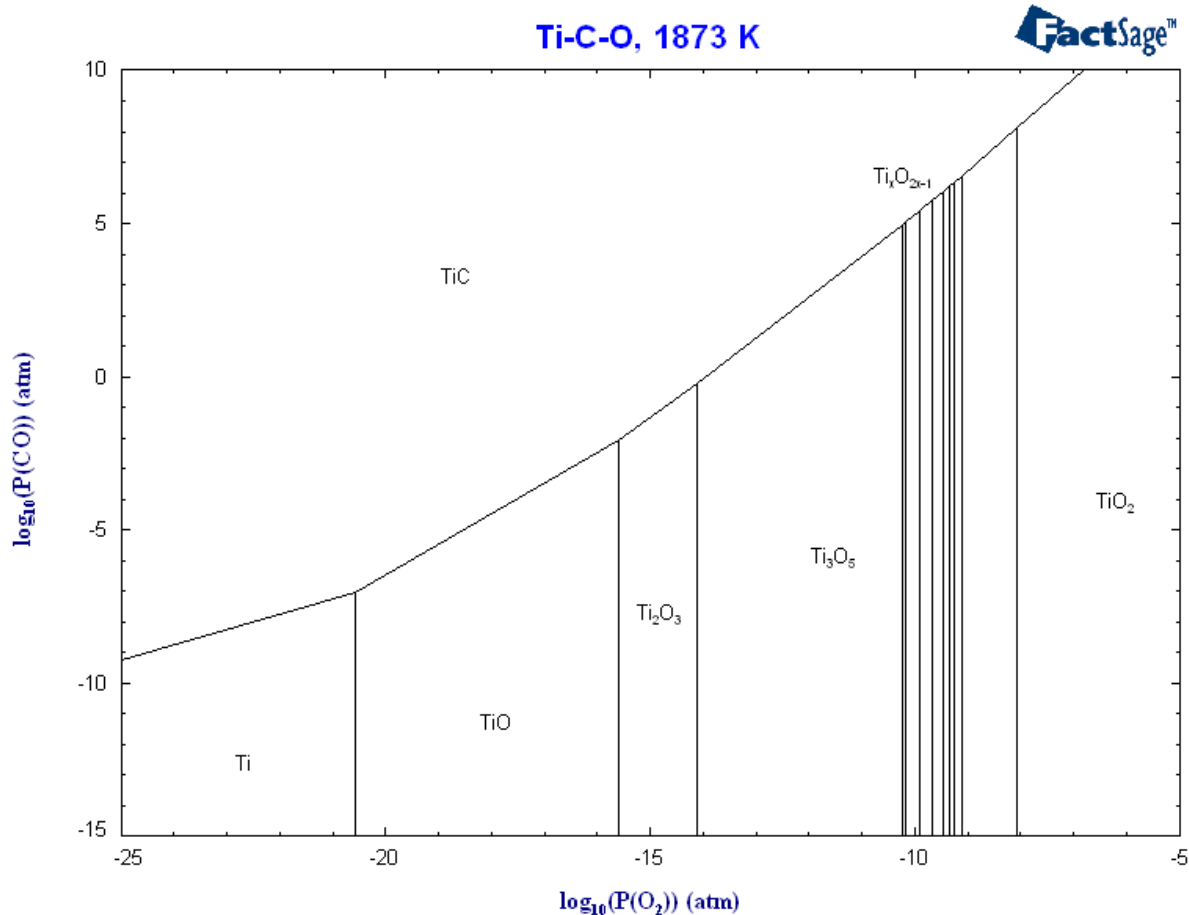


Figure 15: Stability diagram of titanium and its oxides and carbides with partial pressures of oxygen ( $P_{\text{O}_2}$ ) and carbon monoxide ( $P_{\text{CO}}$ ).

## 2.7 Ellingham Diagram for Oxides (Gibb's Free Energy)

The Gibb's free energy for oxidation is a measure of the chemical affinity of the metal for oxygen (Gaskell). Therefore, it can be said that the more negative the Gibb's free energy is, the more stable the oxide is. Figure 16 shows an Ellingham diagram of oxides for titanium and aluminum. The free energy for  $\text{TiO}$  is lower than that of  $\text{Al}_2\text{O}_3$  past  $400^\circ\text{C}$ . The stability ranking then continues from  $\text{Ti}_2\text{O}_3$ ,  $\text{Ti}_3\text{O}_5$  and the least stable oxide  $\text{TiO}_2$ .

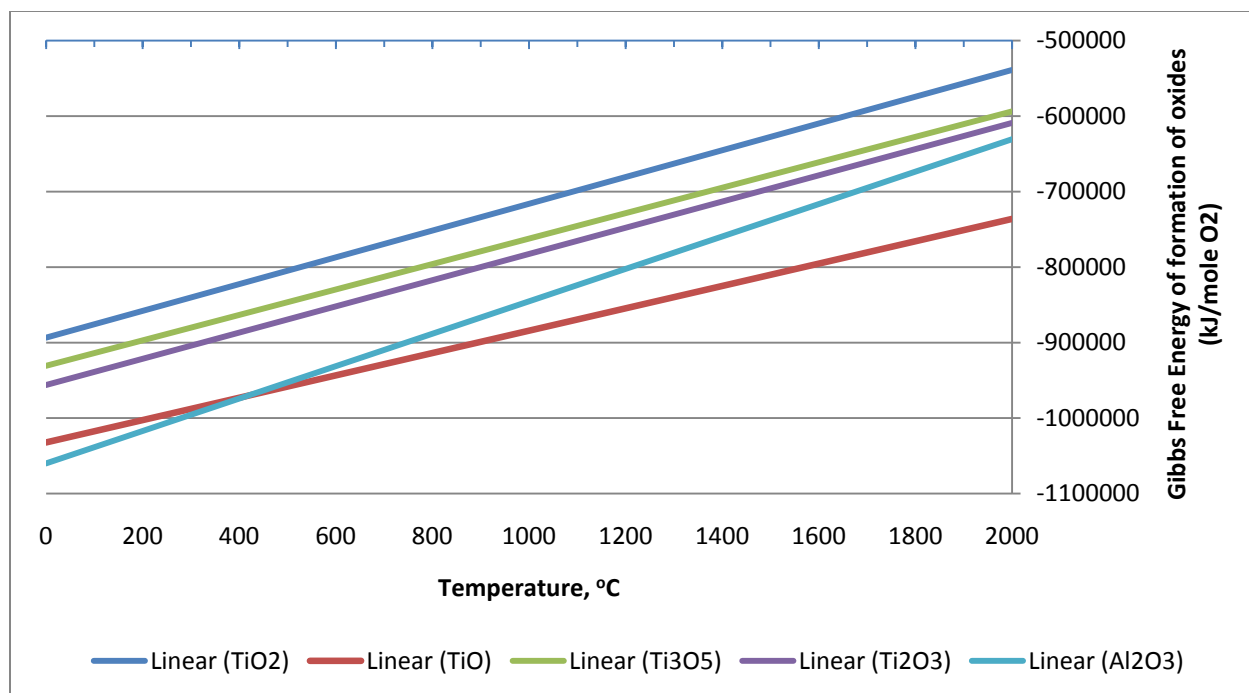


Figure 16: Gibbs free energy of formation of oxides for titanium and aluminum.



## Chapter 3: Research Methodology

### 3.1 Sample Preparation and Experimental System

The samples were prepared according to weight percentages with 99.7%  $\text{TiH}_2$  powder with a particle size of 200 mesh from Atlantic Equipment Engineers and 99.999% aluminum wire with a 0.81 mm diameter from Alfa Aesar. Aluminum powder was avoided as it increases the likelihood of oxidation with the increased surface area exposure to the atmosphere and has a high risk factor associated to its combustibility during high temperature furnace operation. The sample compositions consisted of 70, 73, 75, 78 and 80 wt% Al with the remaining composition being Ti. A duplicate composition of 75 wt% Al was prepared totaling six samples per experiment. Alumina ( $\text{Al}_2\text{O}_3$ ) and partially stabilized zirconia ( $\text{ZrO}_2$ -8 wt%  $\text{Y}_2\text{O}_3$ ) crucibles with the following dimensions: 18.1 mm outer diameter (OD), 15.4mm inner diameter (ID) and a 25.8mm height (5 mL capacity), were used to hold the compositions.

The aluminum wire was rolled cylindrically to fit within the crucibles to easily manage 5 g samples.  $\text{TiH}_2$  powder was poured directly over the aluminum wire, and the crucible was lightly shaken to allow the  $\text{TiH}_2$  to settle within the wire's crevices. Each crucible was notched with a diamond saw along the rim to note the contents of each crucible. A larger  $\text{Al}_2\text{O}_3$  crucible with a 59 mm OD, 54 mm ID and 103 mm height (250 mL capacity) was used to house the smaller crucibles. Three 5 mL crucibles were laid at the bottom of the 250 mL crucible. A  $\text{ZrO}_2$  disc was used to separate the remaining three compositions over the bottom three crucibles. The  $\text{ZrO}_2$  disc also prevented any molten metal to leak into the lower level crucibles in case the  $\text{ZrO}_2$  crucibles failed during heating. Figure 17 shows a diagram of how the crucibles were arranged. A hollow alumina tube with an 88.9 mm OD, 76.2 mm ID and a 1.6 m length was placed within a CM Furnaces 1830-10 vertical tube furnace with a fiber insulation hotface. With the alumina

tube inside the furnace, various alumina crucibles were inserted from underneath the tube along with the sample containing crucible. The alumina crucibles with varying dimensions all fit well within the alumina tube and were used as spacers to accurately place the sample crucible within the furnace's hot zone. The spacer crucibles that sat on top of the sample crucible were used as heat shields or thermal mass loads to prevent the alumina tube from excessive heating during operation as shown in Figure 18.

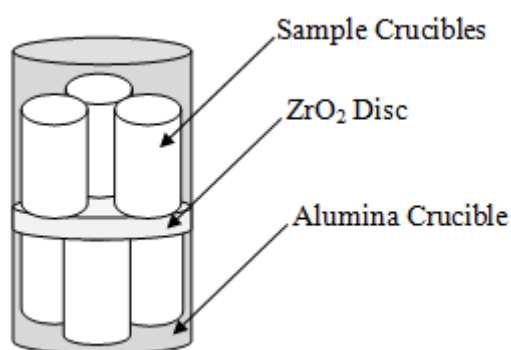


*Figure 17: Simple diagram showing the arrangement of the sample crucibles within the larger alumina crucible.*

The hollow alumina tube was equipped with cooling jigs at both ends. The cooling jigs are metal caps that contain a rubber gasket to create a seal between the alumina tube and the atmosphere. It also has a hose clamp to fasten the tube to the jig, a copper coil that flows water through the jig to keep the gaskets cool, and a hose adapter at the center to allow argon flow within the tube. Dow Corning vacuum grease was applied on the gasket to prevent a backflow of the surrounding air. The system was also designed to allow argon gas to flow from the bottom of the tube and exit through the top where it was connected to a neoprene tube; the neoprene tube was used due to its low oxygen diffusivity. The argon is expelled into a beaker filled with dibutyl phthalate to again prevent back flow of air.

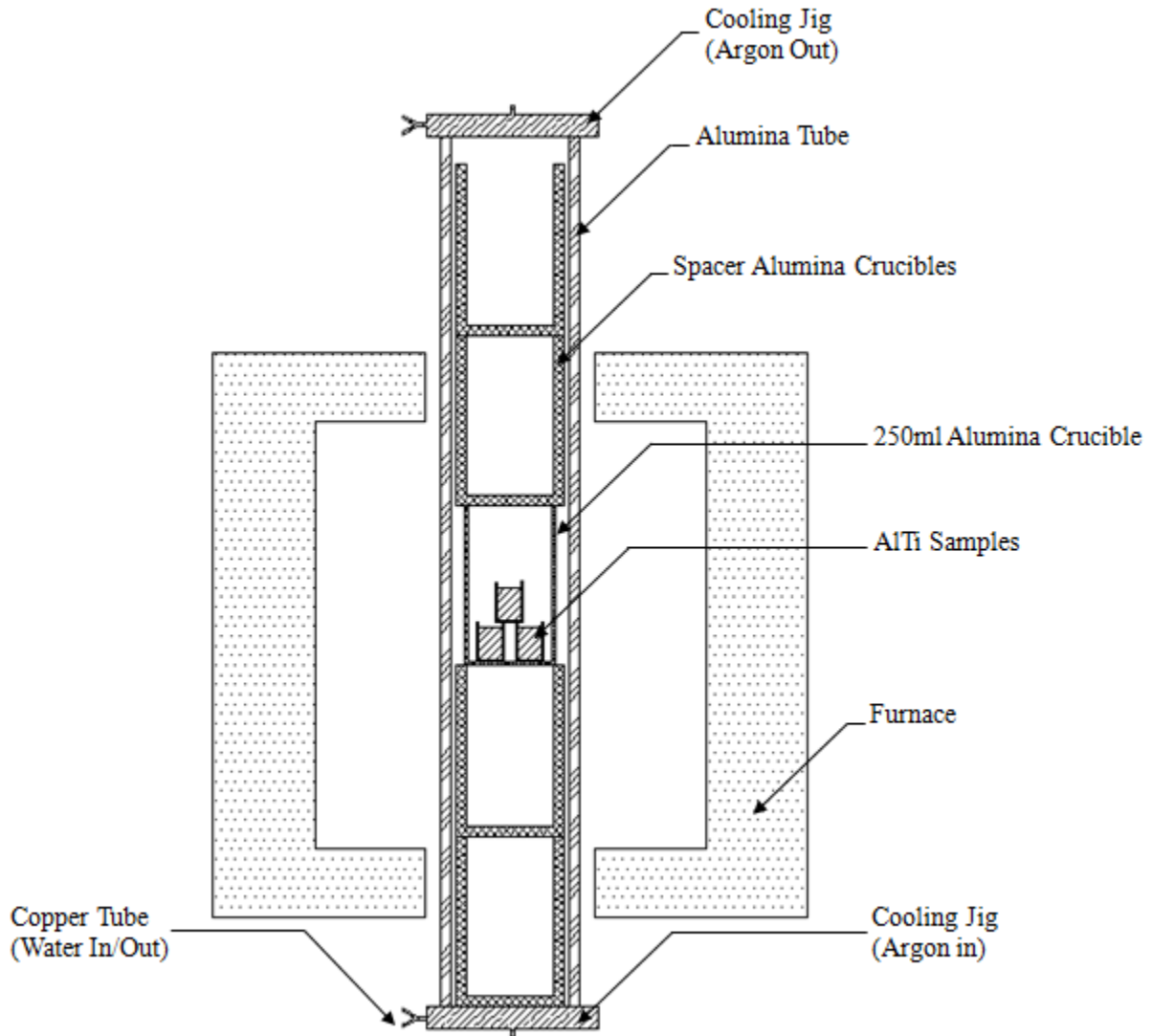


Figure 18: Experiment setup showing an alumina tube within a furnace loaded with the samples.

### 3.2 Argon Purification System

A system of stainless steel and quartz tube were used to direct argon towards the furnace. The samples were exposed to a dehumidified and deoxidized pre-purified argon gas atmosphere. The argon was rated with an oxygen and H<sub>2</sub>O content of less than 3 ppm ( $< 3 \times 10^{-5}$  atm), however that level of contamination is sufficient to create unwanted oxides in the system. Magnesium perchlorate Mg(ClO<sub>4</sub>)<sub>2</sub> was used as a desiccant to remove moisture from the argon.

The argon was then channeled through an oxygen purification system of two smaller electrical furnaces that contained titanium sponge and finally passed through one final  $\text{Mg}(\text{ClO}_4)_2$  desiccant filter. Quartz tube was used to hold the desiccant and titanium sponge. An adapter connected the quartz and stainless steel tubing, and high vacuum grease was applied over the adapter to prevent backflow oxygen contamination. An average of 64.5 g of Ti sponge fit into the first furnace and 42.9 g Ti in the second. With the furnaces operating at 700°C and 850°C, the total  $P_{\text{O}_2}$  in the system was reduced to  $10^{-32}$  atm preventing formation of aluminum and titanium oxides within the system at an operating temperature of 1600°C. The argon then flowed through the hollow alumina tube where it was exposed to the samples inside the furnace. A basic flow diagram is shown in Figure 19 that quickly describes the processes that the argon undergoes.

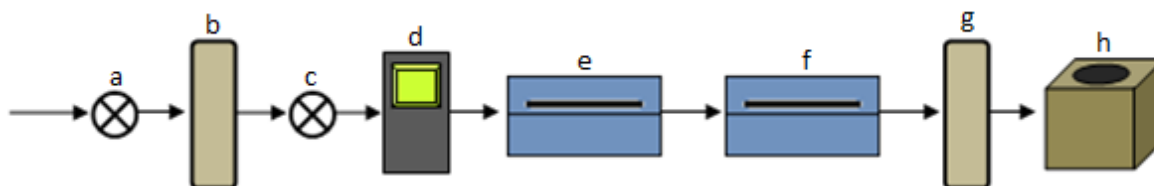


Figure 19: The flow of argon. a) valve, b)  $\text{Mg}(\text{ClO}_4)_2$ , c) needle valve, d) flow meter, e) furnace at 850°C, f) furnace at 700°C, g)  $\text{Mg}(\text{ClO}_4)_2$ , h) tube furnace

### 3.3 Experimental Procedure

When the samples were loaded within the vertical tube furnace, the system was allowed to flush out air that had been trapped within the system during the setup. Two chromel furnaces at 700°C and 850°C filled with titanium sponge were used to further purify the argon. The titanium absorbs oxygen from the system creating an arrangement of oxides ( $\text{TiO}$ ,  $\text{Ti}_2\text{O}_3$ ,  $\text{Ti}_3\text{O}_5$ , and  $\text{TiO}_2$ ). The formation of these oxides prior to being introduced to the samples reduces the  $P_{\text{O}_2}$  of the system to  $10^{-32}$  atm, according to Ti/TiO equilibrium, where neither titanium nor

aluminum will oxidize. The system was flushed for 3 hours with the purified argon gas. After the flushing period, the vertical tube furnace was set at a ramp rate of 200°C/hr. The ramp rate was designated as such to prevent the alumina tube from cracking due to the differential thermal expansion caused by the temperature gradient from the alumina tube that is exposed to the atmosphere and the section within the furnace. When the furnace reached an operating temperature of 1600°C, the samples were given 4 hours to homogenize. The resulting samples were allowed to cool within the furnace over night.

After the samples were extracted from the furnace, the sample crucibles were cut longitudinally in half with a diamond saw. The samples were mounted in a 1.25” sample mold with an epoxy resin. Once the resin had cured the samples were prepared for metallography by polishing the samples with silicon carbide discs with grit sizes of 80, 120, 400, 600, 800, 1000, and 1200. The sample were given a final polish with a polishing cloth and 1 µm diamond paste and rinsed clean with methanol. The resulting samples were examined under a Reichert MEF 4M optical microscope and the compositions were analyzed with a Bruker X-Ray Diffractometer (XRD) for d-spacing evaluation.

## Chapter 4: Results

After the samples were cooled, the 250mL crucible was extracted from the furnace. The samples that were loaded in  $\text{ZrO}_2$  crucibles showed cracking, but the compositions were not compromised as they did not leak. White spots were visible on the top of the samples, evidence of surface oxidation. Upon cutting the samples, the Ti-78 wt% Al contained a large void. A small button was adhered to the bottom of the crucible and the remaining composition appeared to be floating; both of the portions were analyzed for metallography and x-ray diffraction. The button is labeled “button” and the remaining sample portion “cover” when referred to. A duplicate of Ti-75 wt% Al was made during the experiment. The sample that was placed below the  $\text{ZrO}_2$  disc (refer back to Figure 17) is labeled “bottom” and the other sample “top.” An attempt was made to obtain darkfield images of the sample, but the results showed no differential contrast in the observed samples.

The samples were analyzed with x-ray diffraction. The Bruker diffractometer was equipped with a 6.0 mm slit x-ray emitter and an 8.0 mm detector. The 2-theta scanning range was initially set to  $20^\circ$ - $90^\circ$  with a step size of 0.05 on a continuous scan setting speed of 6 degrees per minute. The results varied per sample orientation and several scans were taken of each sample. The scans were then merged to give an overall characterization of the d-spacing peak profile of the samples. The individual scans and the merged scan can be seen in Figures 27-33 to show the comparison of each scan.

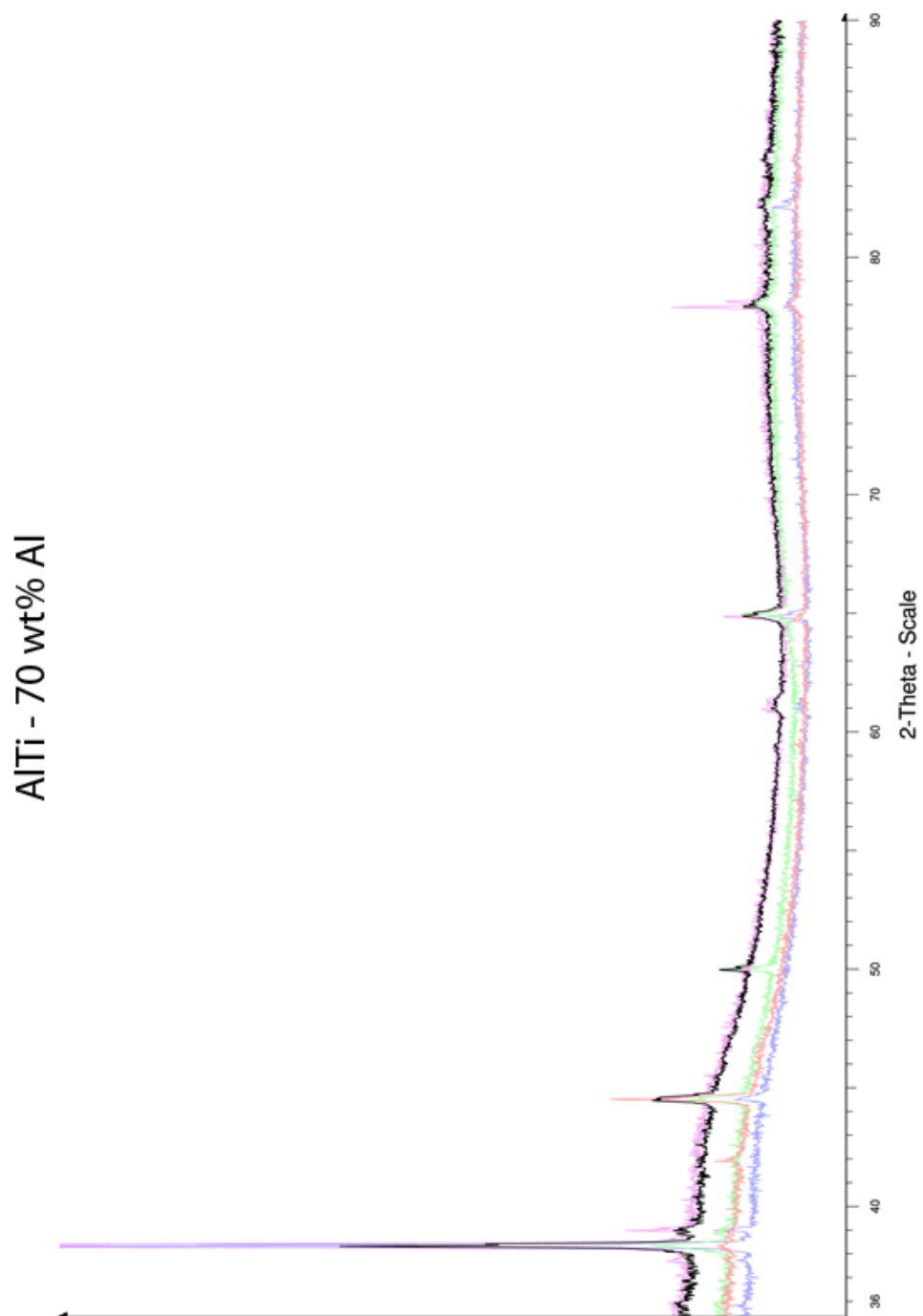


*Figure 20: XRD profile for several scans for Ti-70 wt% Al. The dominant black scan is the final characteristic scan.*

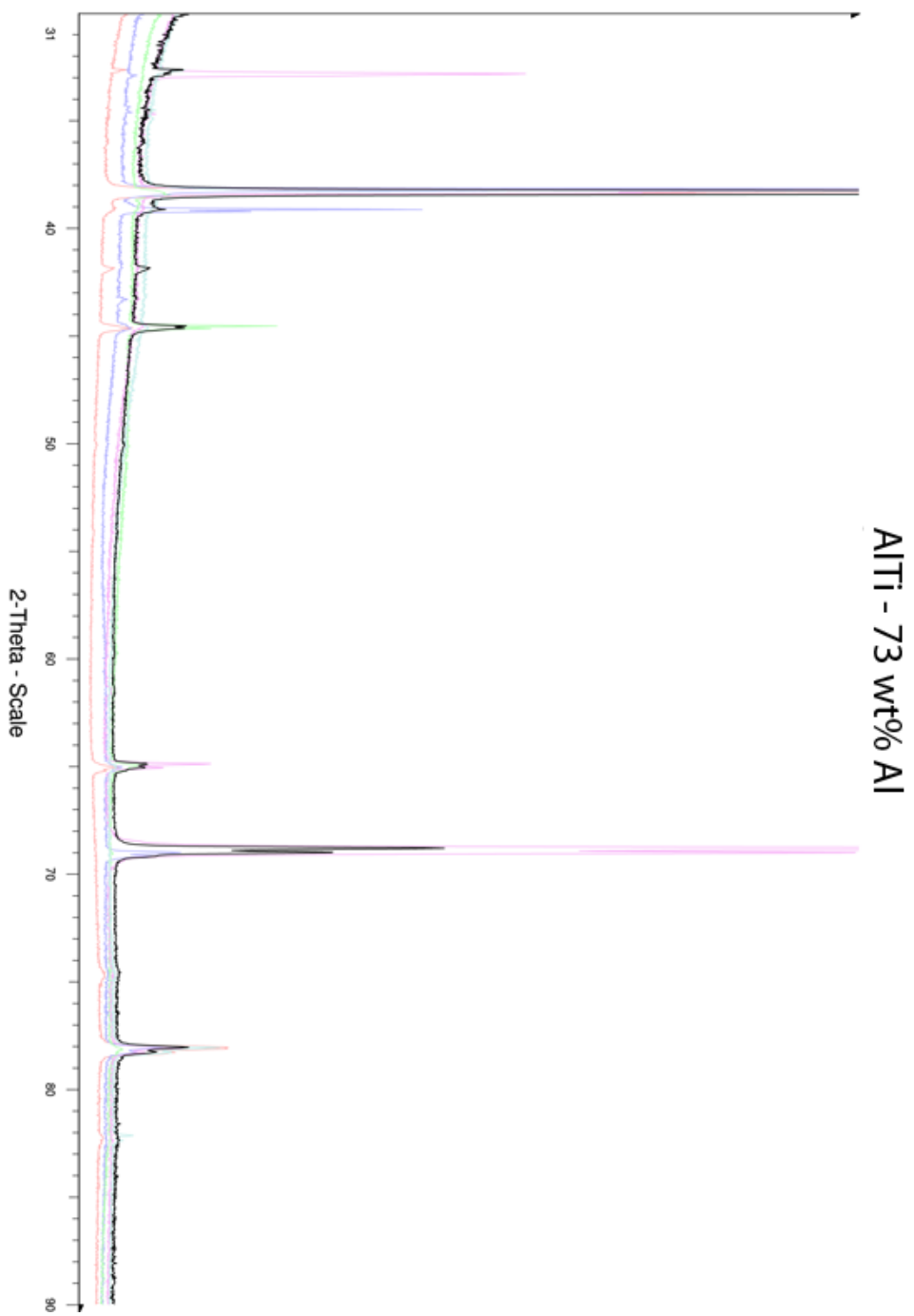


*Figure 21: XRD profile for several scans for Ti-73 wt% Al. The dominant black scan is the final characteristic scan.*



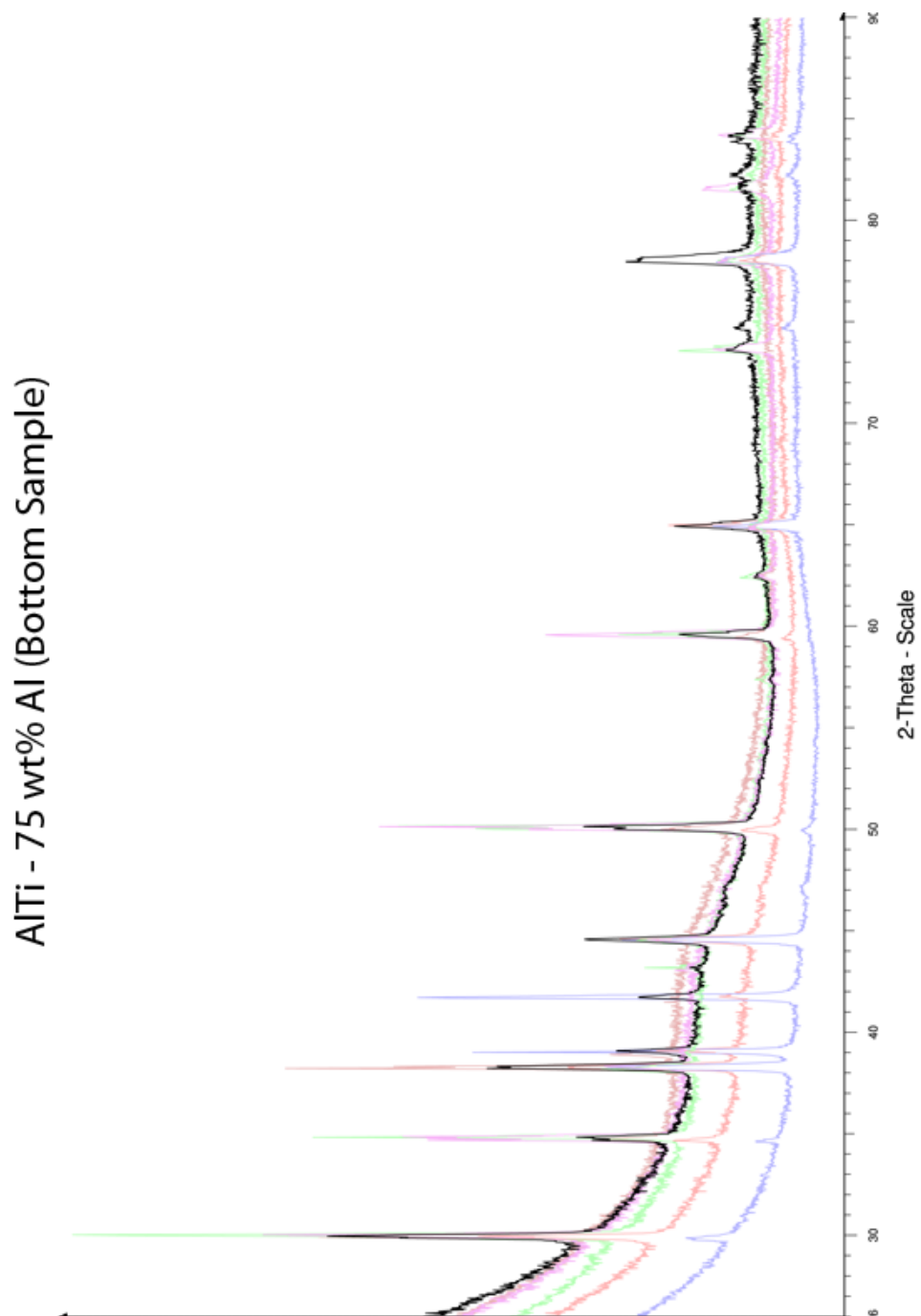
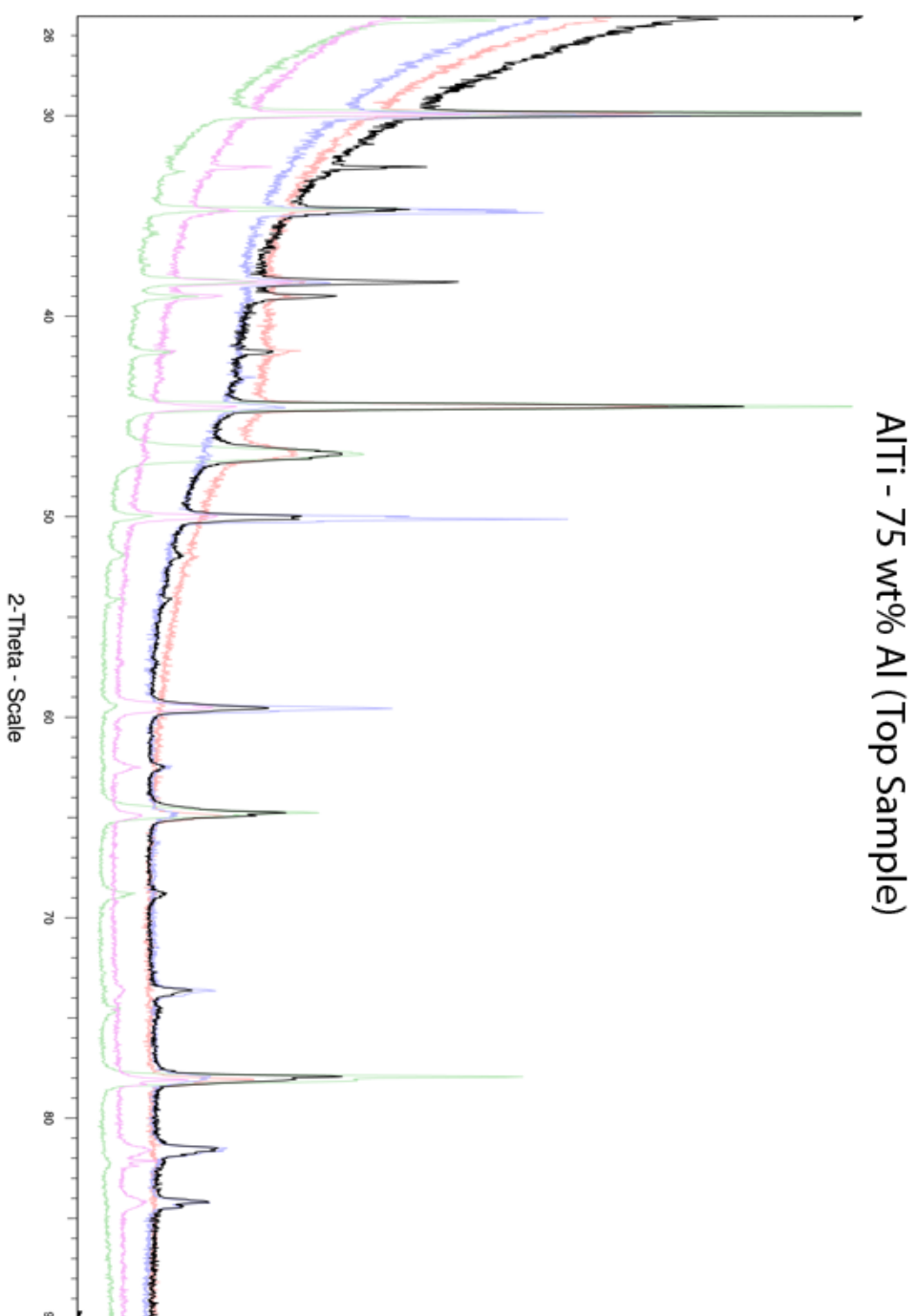


Figure 22: XRD profile for several scans for Ti-75 wt% Al (bottom sample). The dominant black scan is the final characteristic scan.



*Figure 23: XRD profile for several scans for Ti-75 wt% Al (top sample). The dominant black scan is the final characteristic scan.*

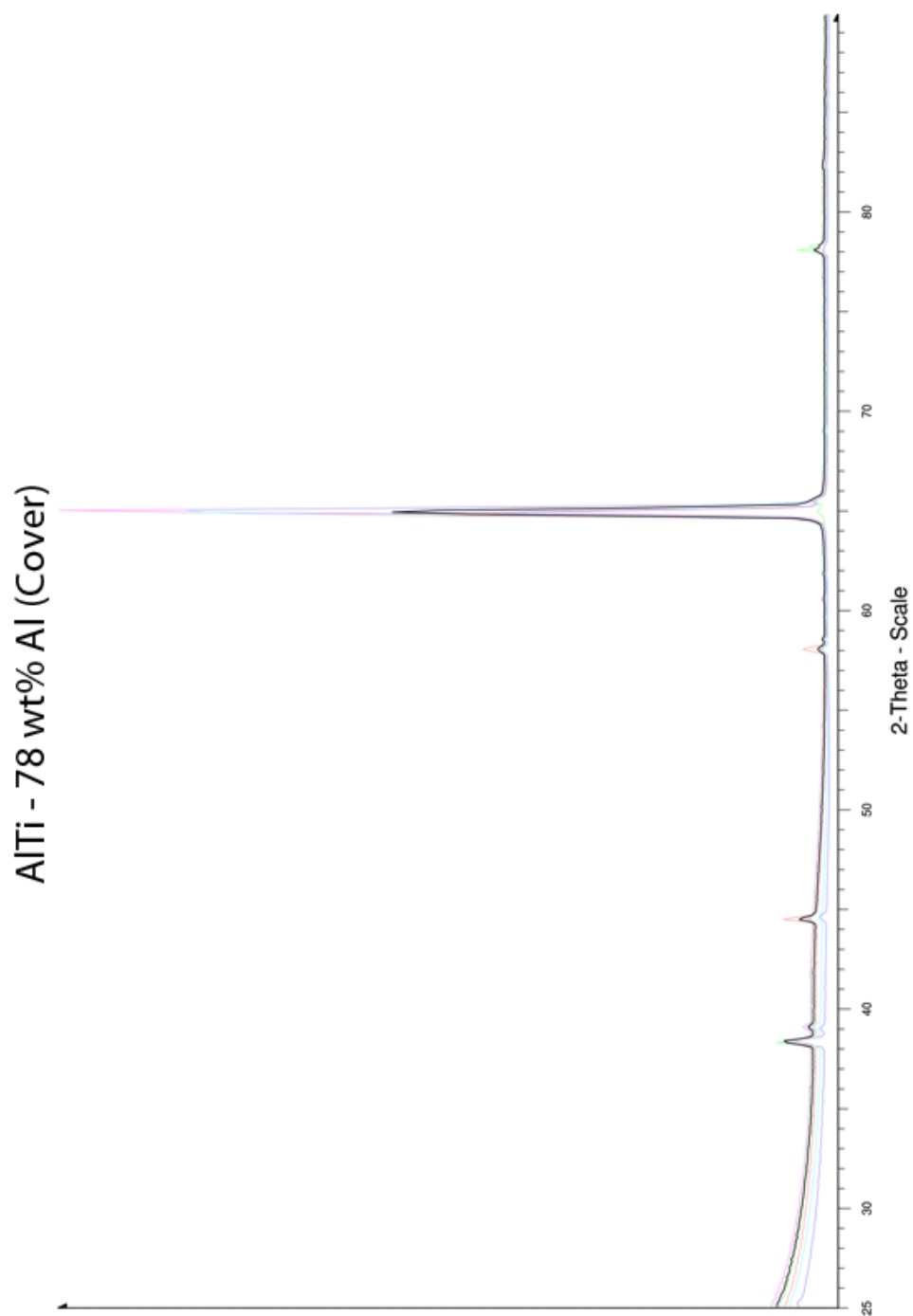
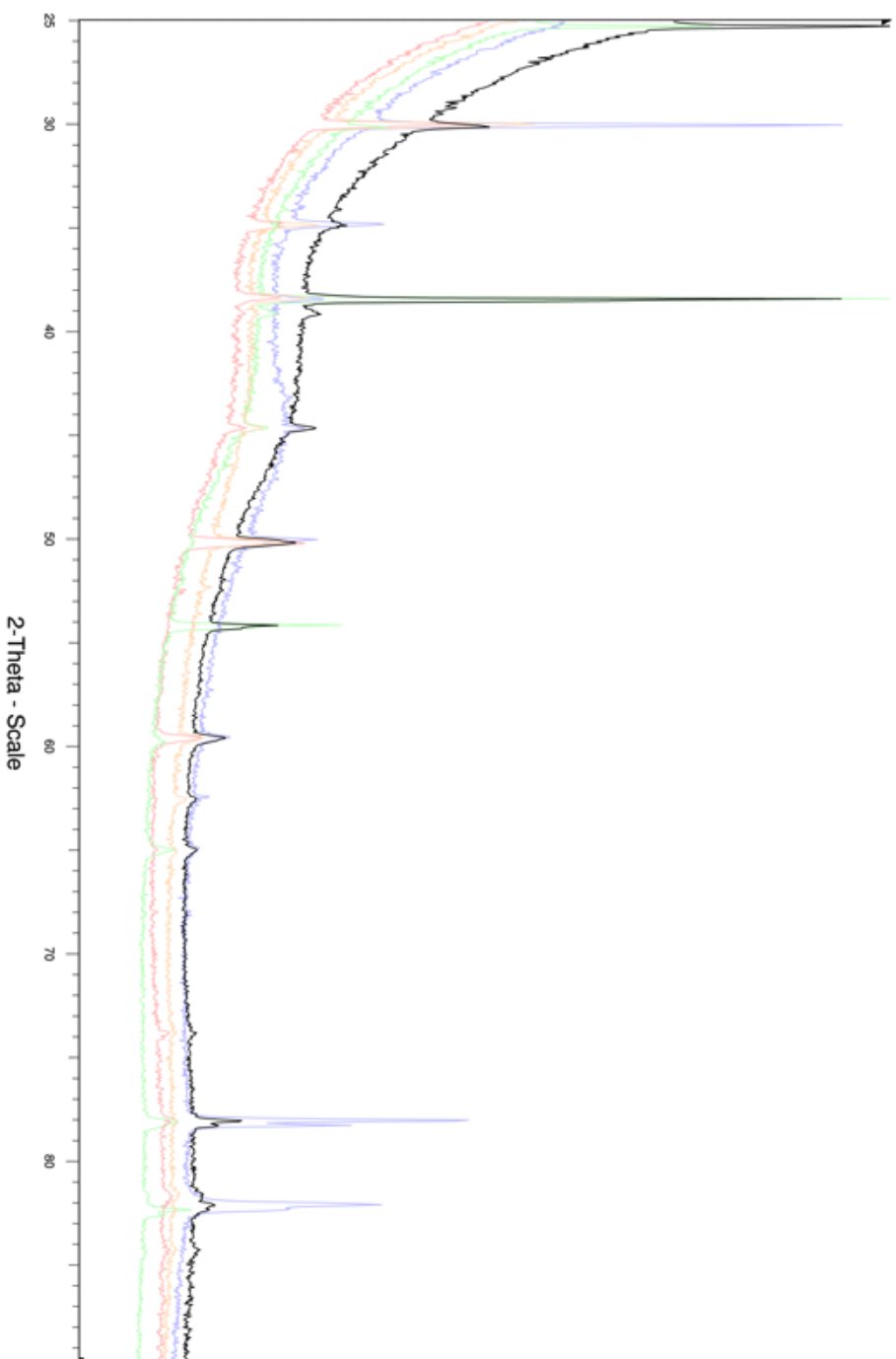
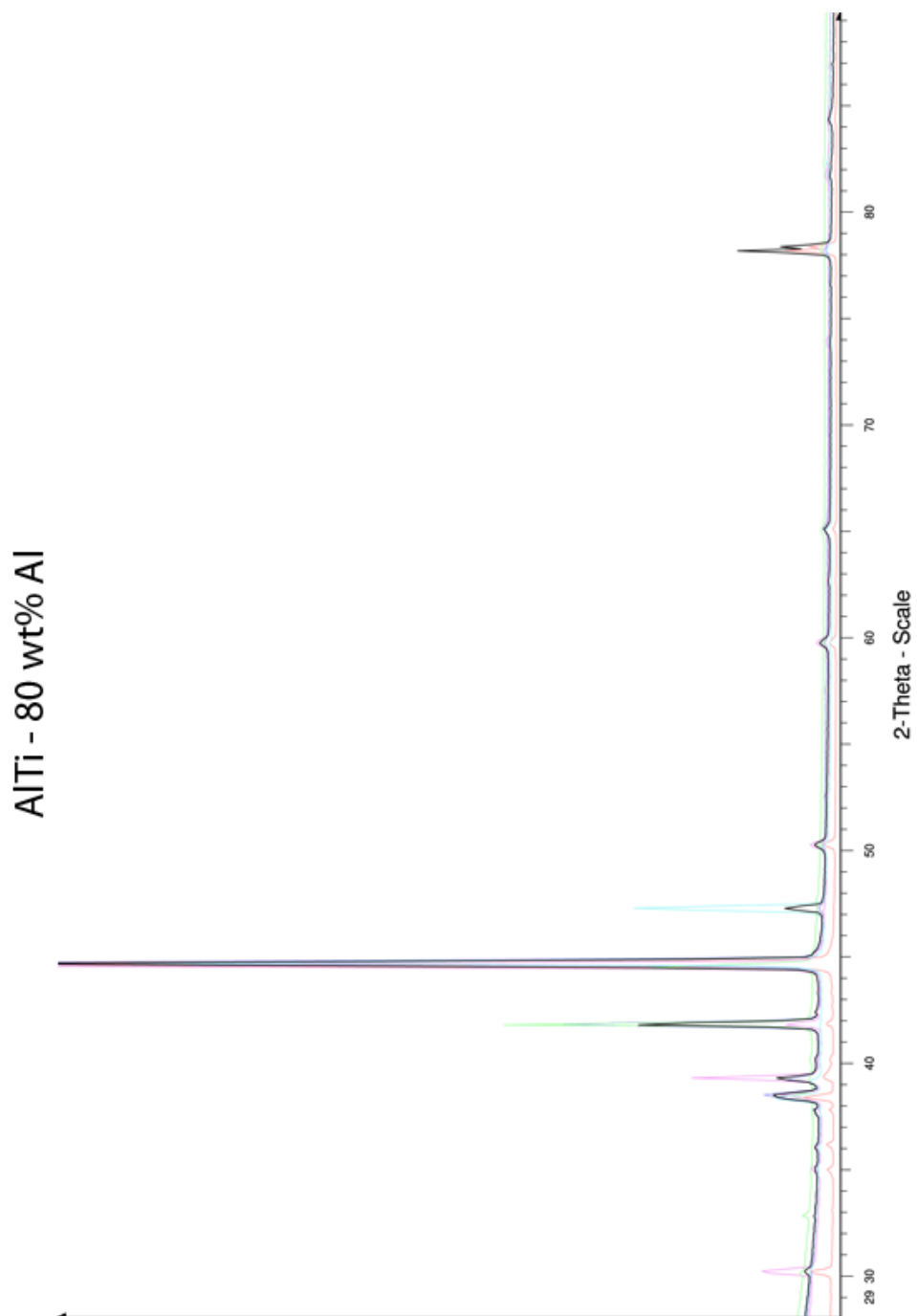


Figure 24: XRD profile for several scans for Ti-78 wt% Al (cover). The dominant black scan is the final characteristic scan.

### AlTi - 78 wt% Al (button)



*Figure 25: XRD profile for several scans for Ti-78 wt% Al (button). The dominant black scan is the final characteristic scan.*



*Figure 26: XRD profile for several scans for Ti- 80 wt% Al. The dominant black scan is the final characteristic scan.*

Peak identification shows a match to fcc-Ti and fcc-Al for all samples. Only the samples that were housed in a ZrO<sub>2</sub> crucible showed the ZrO<sub>2</sub> peaks. Ti-78 wt% Al (cover) did not show ZrO<sub>2</sub>, but the button that was adhered to the bottom of crucible did. Although the same scan settings were used on all of the samples, the intensity profile and the noise level vary between the compositions.

Ti-70 wt% Al displayed high intensity noise levels prior to the first dominant Ti and Al peak in all orientations, therefore the data was omitted. There also exists a peak at 50 degrees that is characteristic of ZrO<sub>2</sub> but no other ZrO<sub>2</sub> peak matches the profile. Ti-73 wt% Al did not have as large a noise level as Ti-70 wt% Al and the full 30°-90° 2-theta scale is shown. Al<sub>3</sub>Ti becomes more prominent in the diffraction scans.

Ti-75 wt% Al (Bottom) and Ti-75 wt% Al (Top) have ZrO<sub>2</sub> and Al<sub>3</sub>Ti peaks. The top sample shows extra Al<sub>3</sub>Ti peaks that are not present in the bottom sample, and the peak intensities for Al and Ti vary. Ti-78 wt% Al (button) has a similar peak profile to Ti-75 wt% Al. The peak profile for Ti-80 wt% Al is similar to the previous ones, but has a reduced noise profile. Ti-78 wt% Al (Cover) also shows very little noise, but the peak intensities have drastically changed. Al<sub>3</sub>Ti is still detected while ZrO<sub>2</sub> is no longer visible. The XRD profiles for each composition with peak identification can be seen in Figures 34-40.

## AlTi - 70 wt% Al - Peak Identification

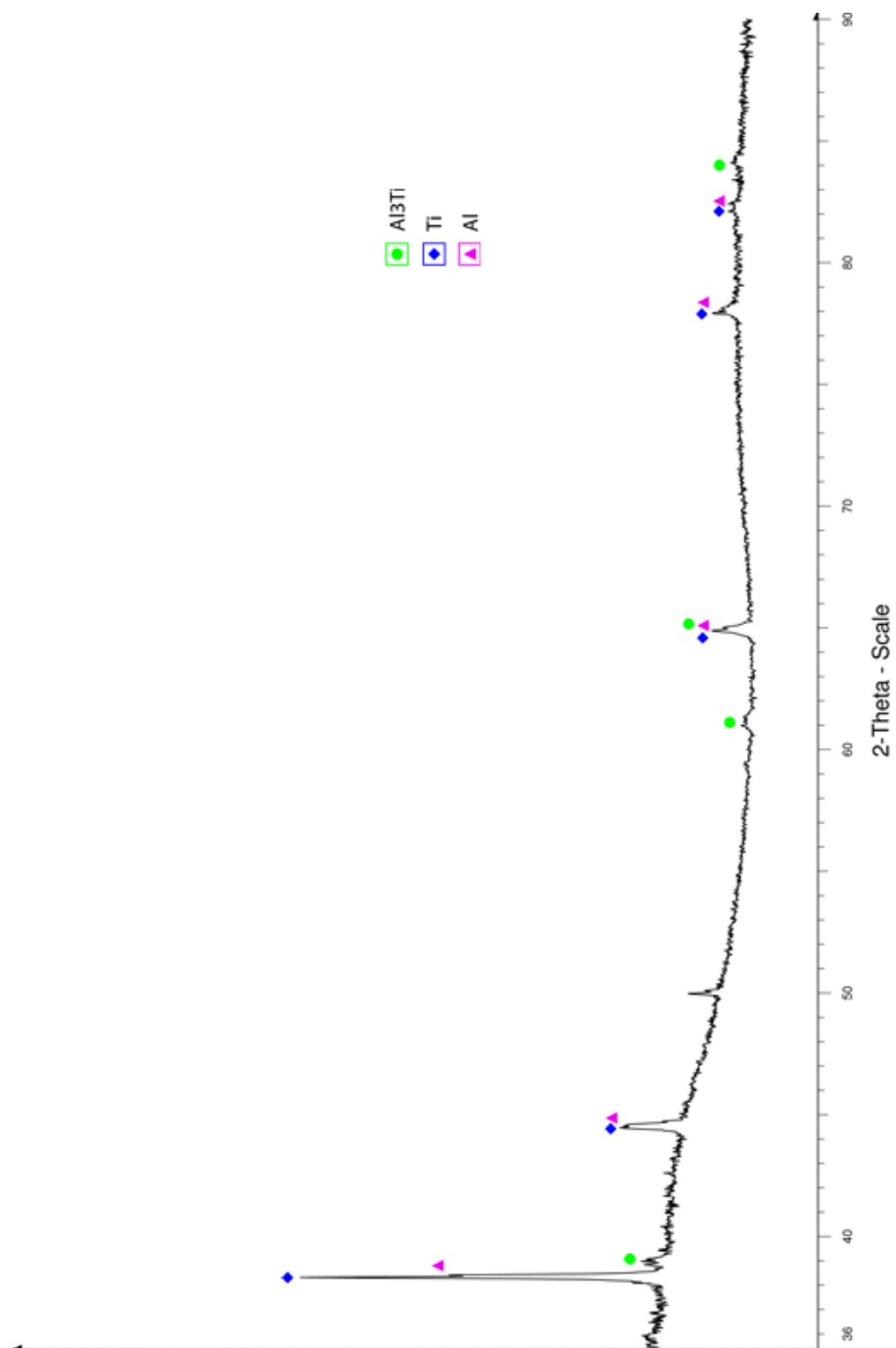


Figure 27: XRD profile for Ti-70 wt% Al with peak identification. Al,  $\text{Al}_3\text{Ti}$ , and Ti are detected.

## AlTi - 73 wt% Al - Peak Identification

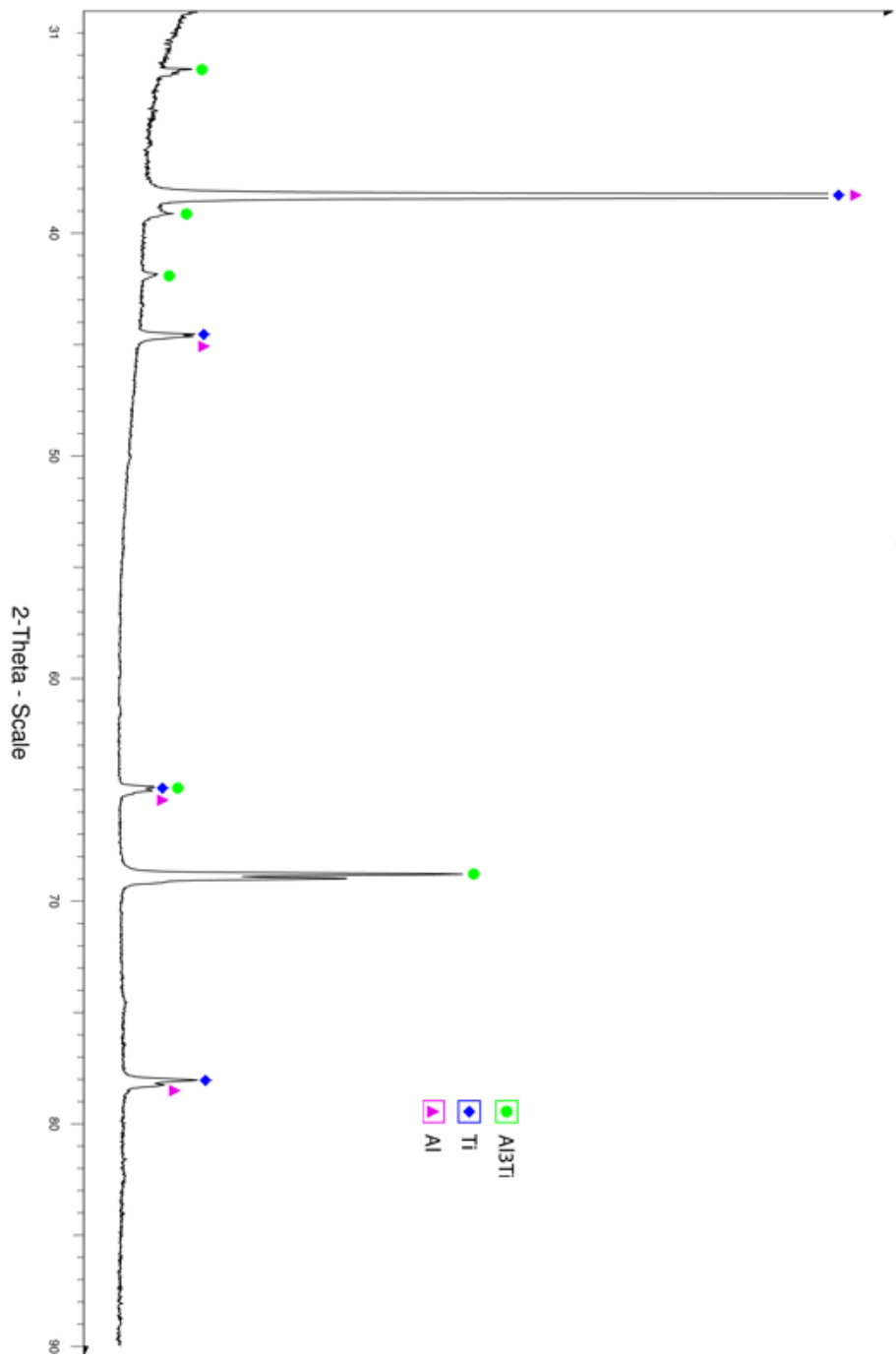


Figure 28: XRD profile for Ti-73 wt% Al with peak identification. Al, Al<sub>3</sub>Ti and Ti are detected.



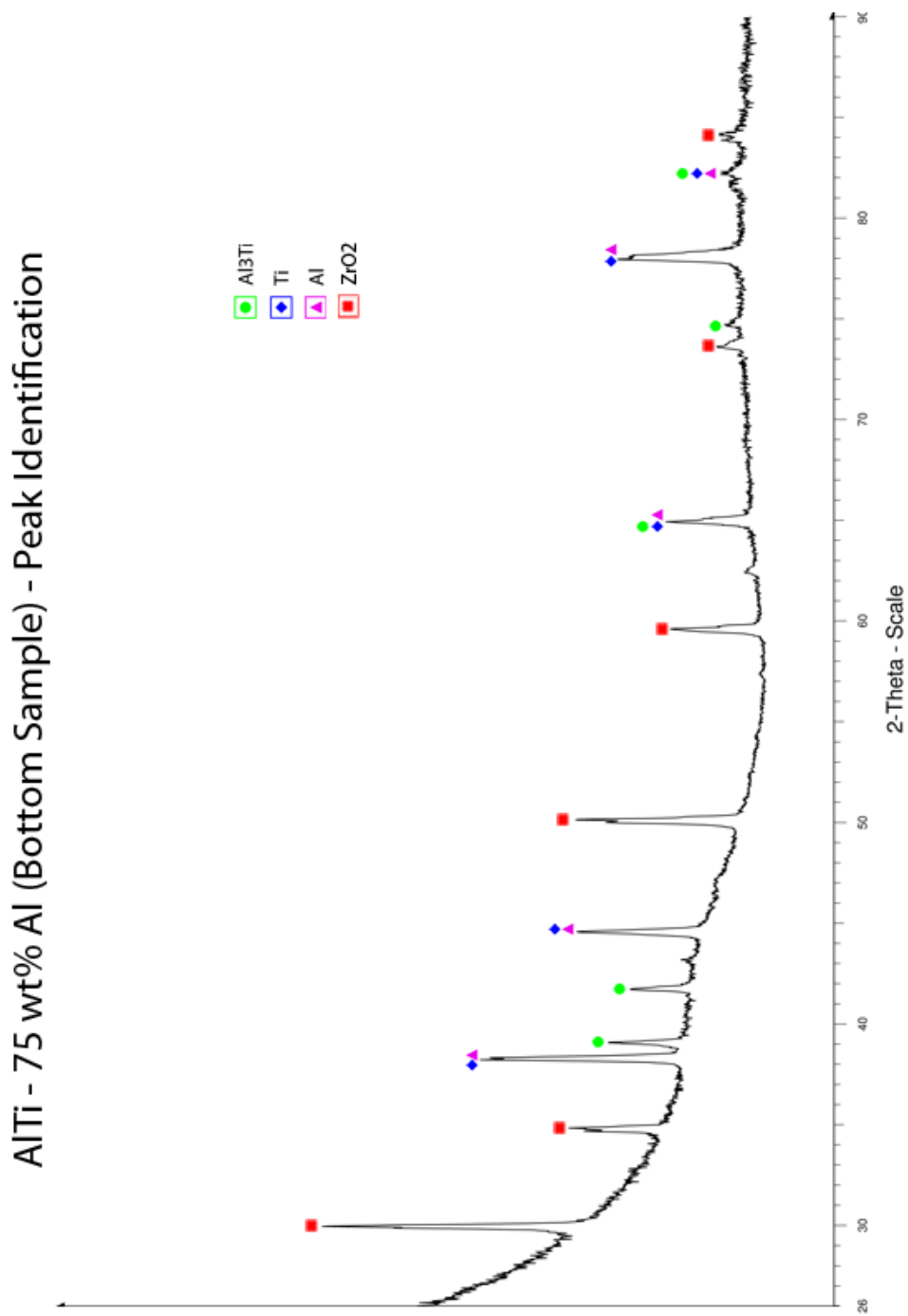


Figure 29: XRD profile for Ti-75 wt% Al (Bottom Sample) with peak identification. Al, Al<sub>3</sub>Ti, Ti and ZrO<sub>2</sub> are detected.

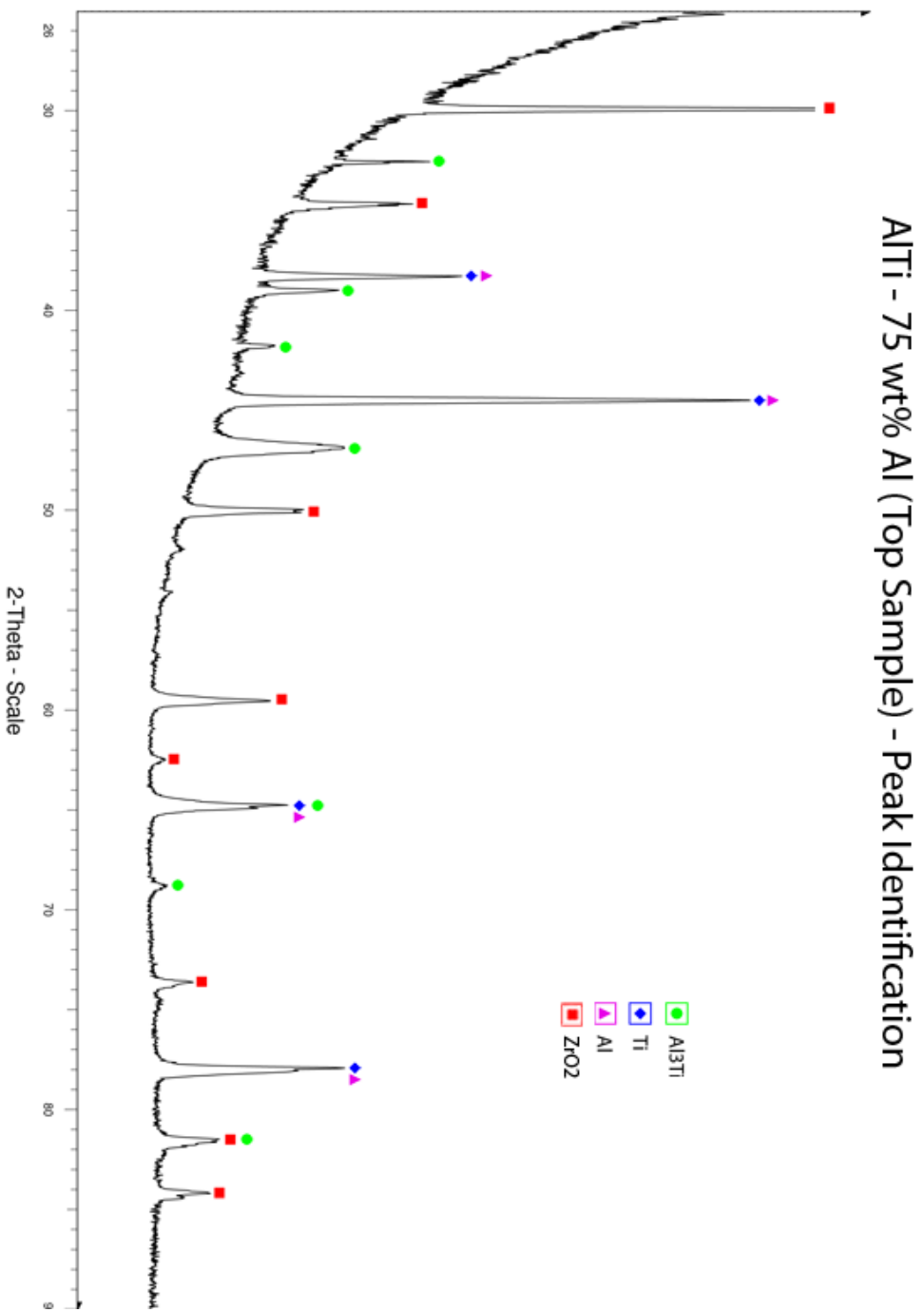


Figure 30: XRD profile for Ti-75 wt% Al (Top Sample) with peak identification. Al, Al<sub>3</sub>Ti, Ti and ZrO<sub>2</sub> are detected.

### AlTi - 78 wt% Al (Cover) - Peak Identification

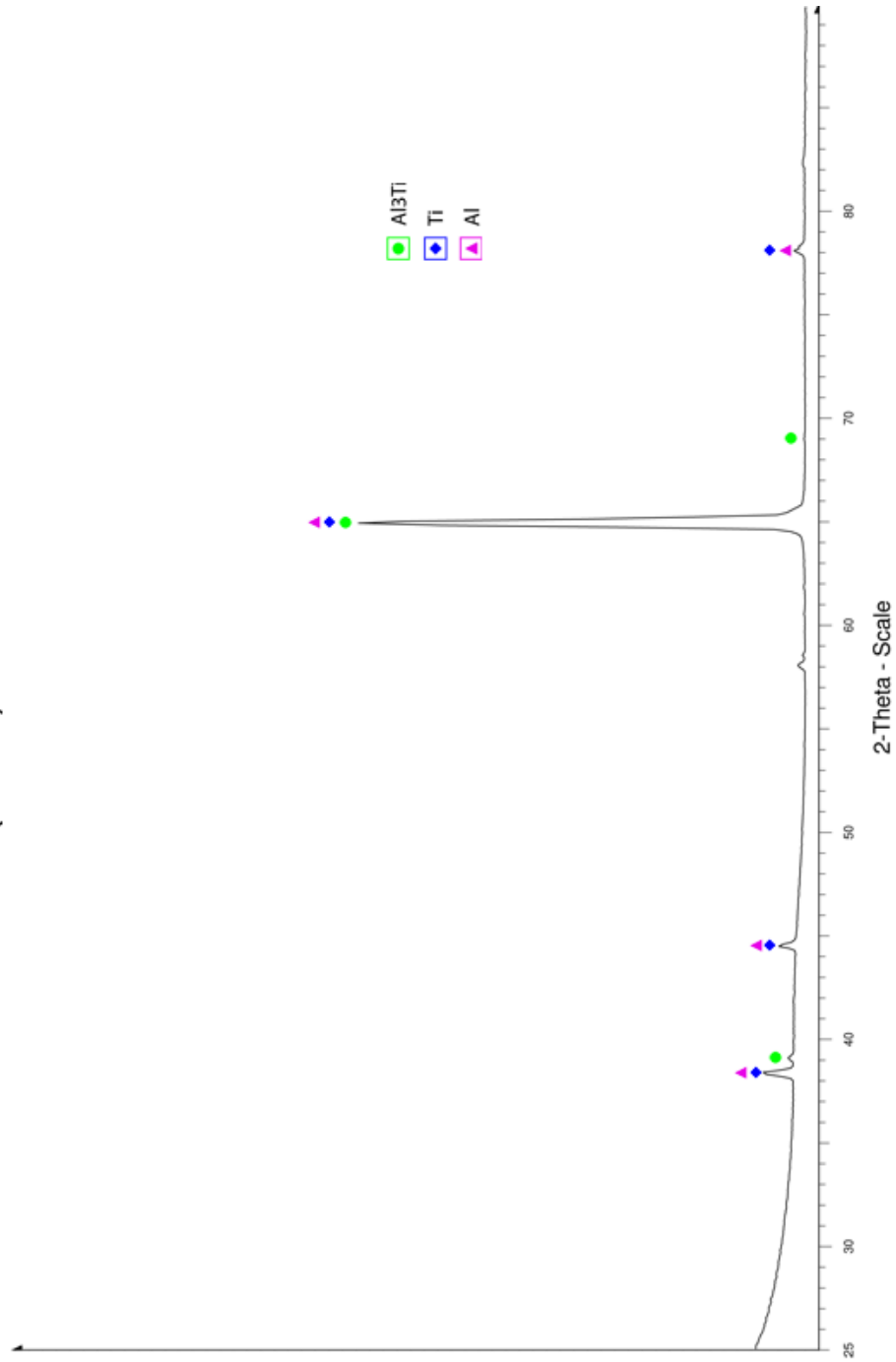
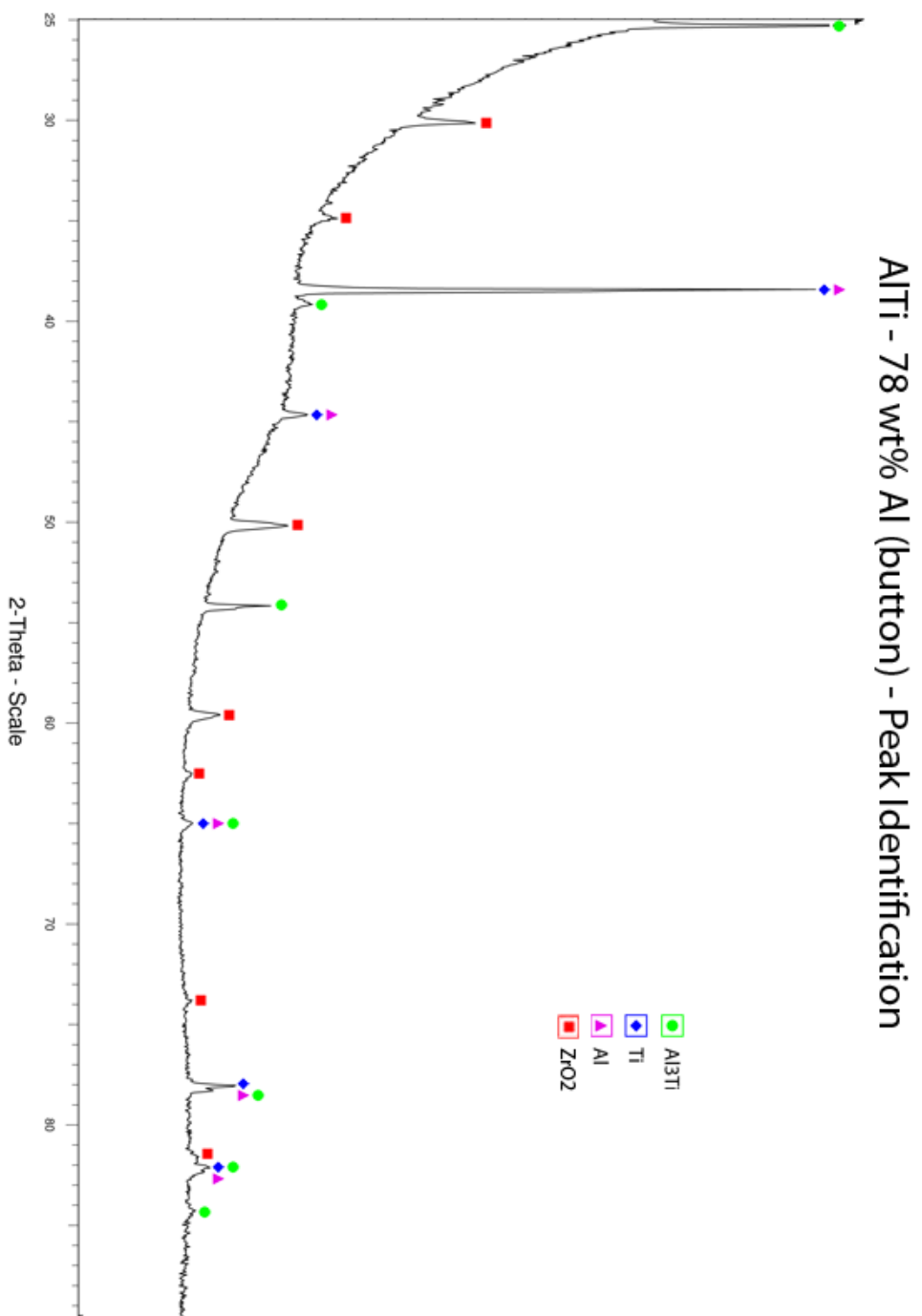


Figure 31: XRD profile for Ti-78 wt% Al (Cover) with peak identification. Al, Al<sub>3</sub>Ti and Ti are detected.



*Figure 32: XRD profile for Ti-78 wt% Al (button) with peak identification. Al, Al<sub>3</sub>Ti, Ti and ZrO<sub>2</sub> are detected.*

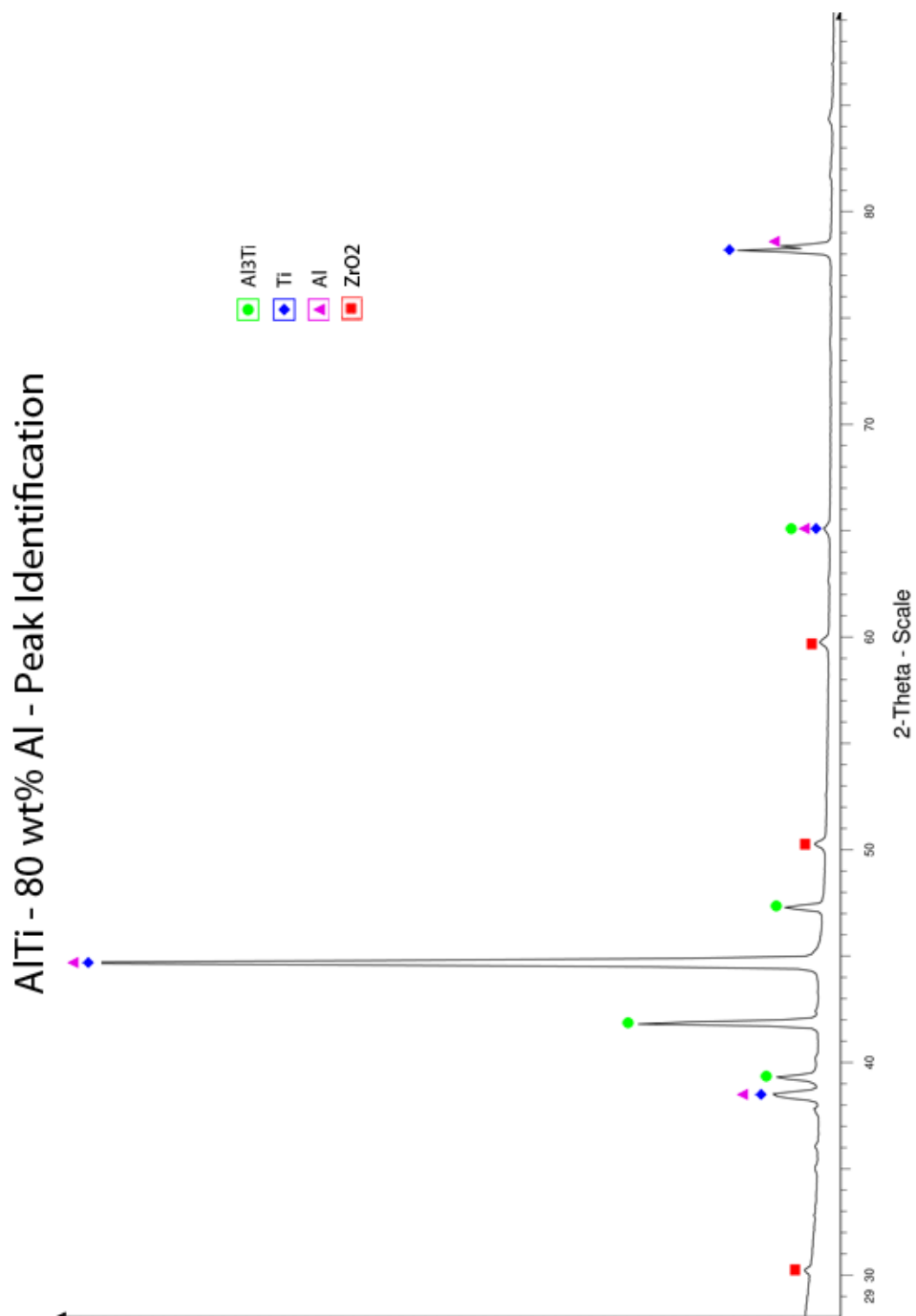
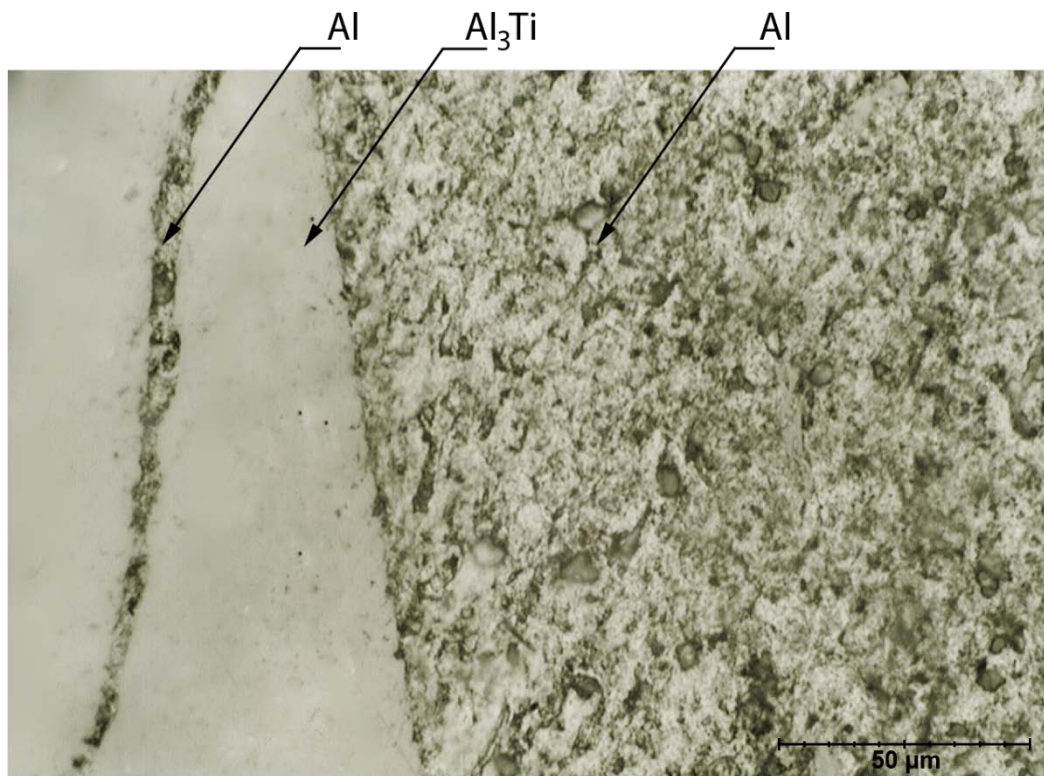
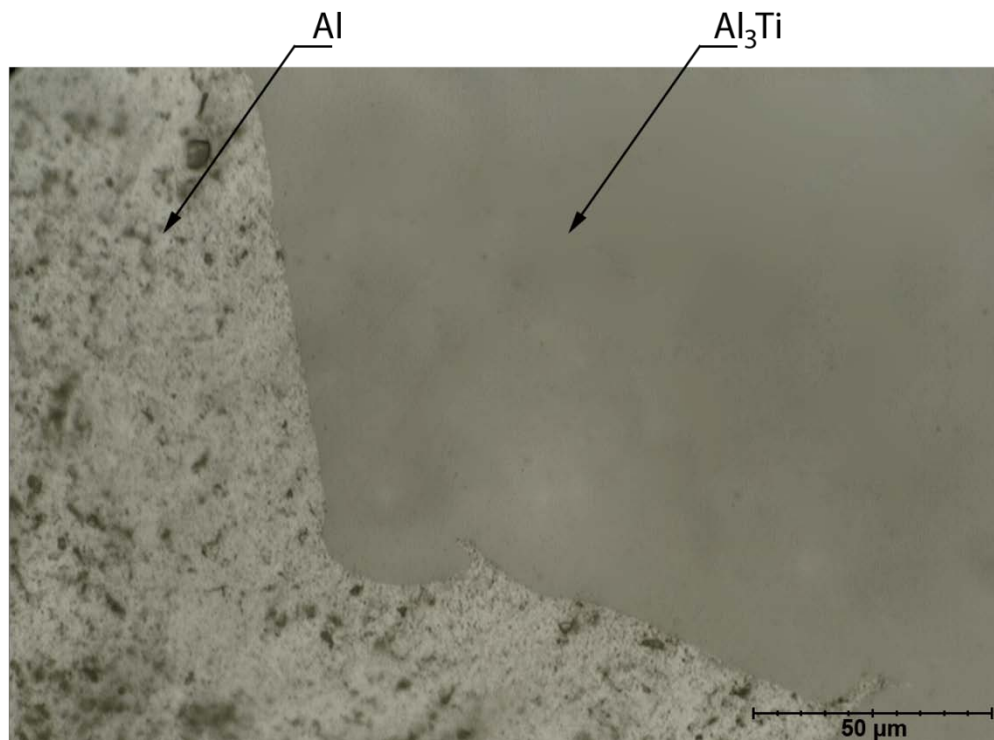


Figure 33: XRD profile for Ti-80 wt% Al with peak identification. Al, Al<sub>3</sub>Ti, Ti and ZrO<sub>2</sub> are detected.

All the samples exhibited elongated crystals with no preferred orientation surrounded by a grainy metal matrix. From analyzing the microstructure, it is evident the grainy matrix surrounding the elongated crystals become finer as aluminum content increases or as titanium hydride content decreases. The microstructures are shown in Figures 20-26. According to the Ti-Al phase diagram, it is expected to see  $\text{TiAl}_3$  either in the high (h) or low temperature (l) phase and Al.



*Figure 34: Microstructure for titanium aluminide – 70 wt% Al.*



*Figure 35: Microstructure for titanium aluminide – 73 wt% Al.*

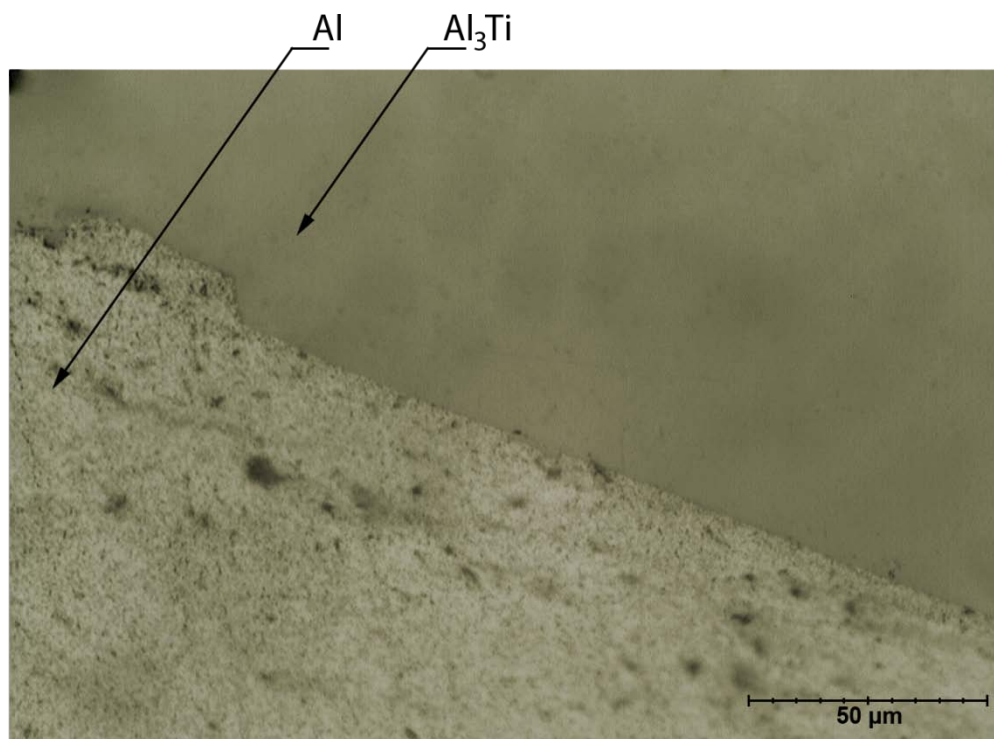


*Figure 36: Microstructure for titanium aluminide – 75 wt% Al. This composition was located on the bottom layer.*

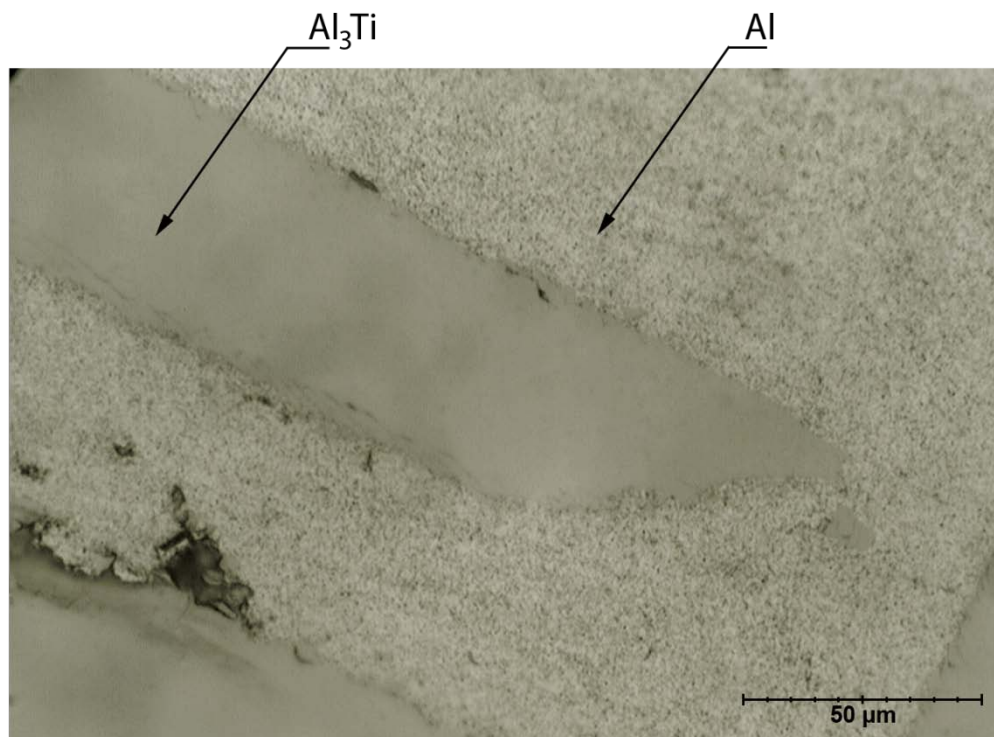


*Figure 37: Microstructure for titanium aluminide – 75 wt% Al. This composition was on the top layer.*

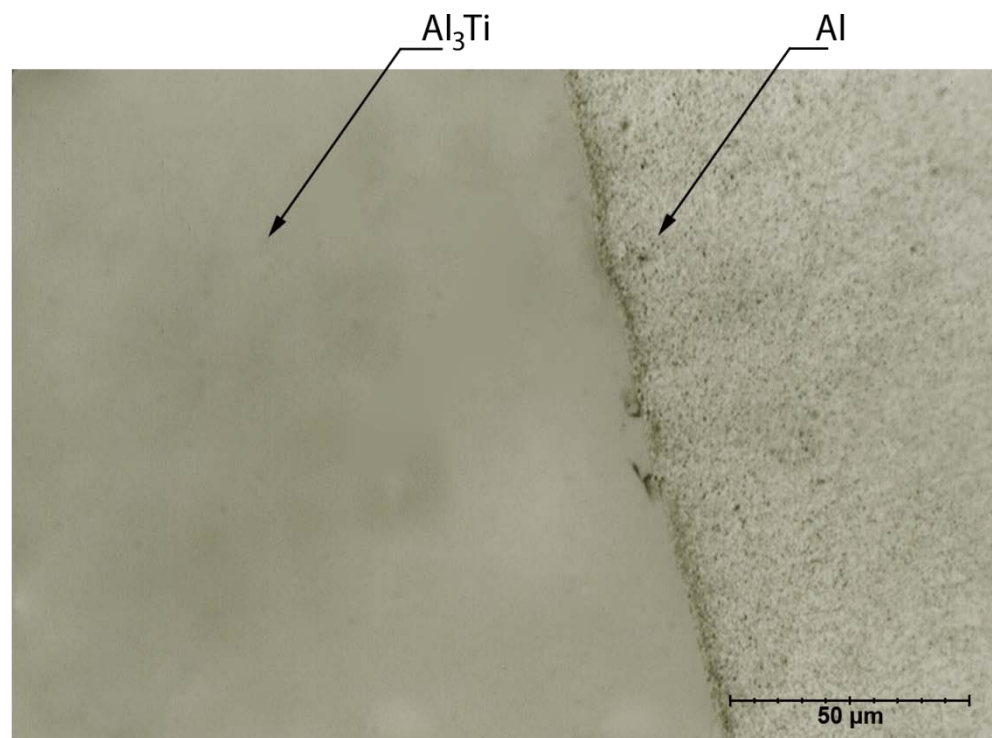


*Figure 38: Microstructure for titanium aluminide – 78 wt% Al. This composition was the top layer of the sample.*



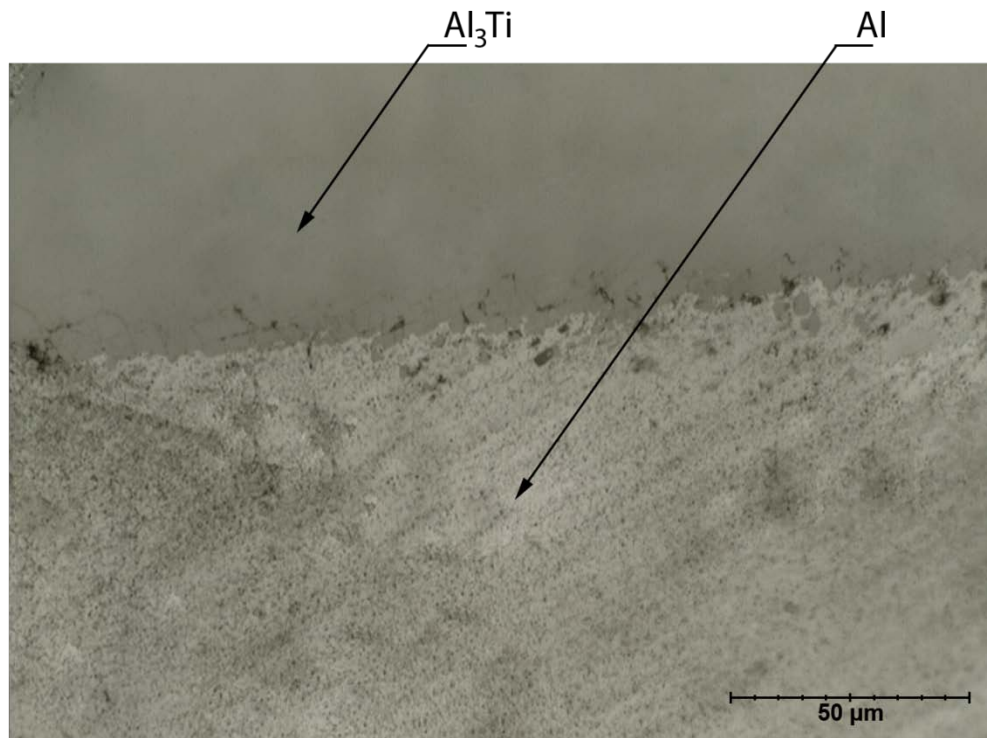


*Figure 39: Microstructure for titanium aluminide – 78 wt% Al. This composition was the button that lay on the bottom of the crucible.*

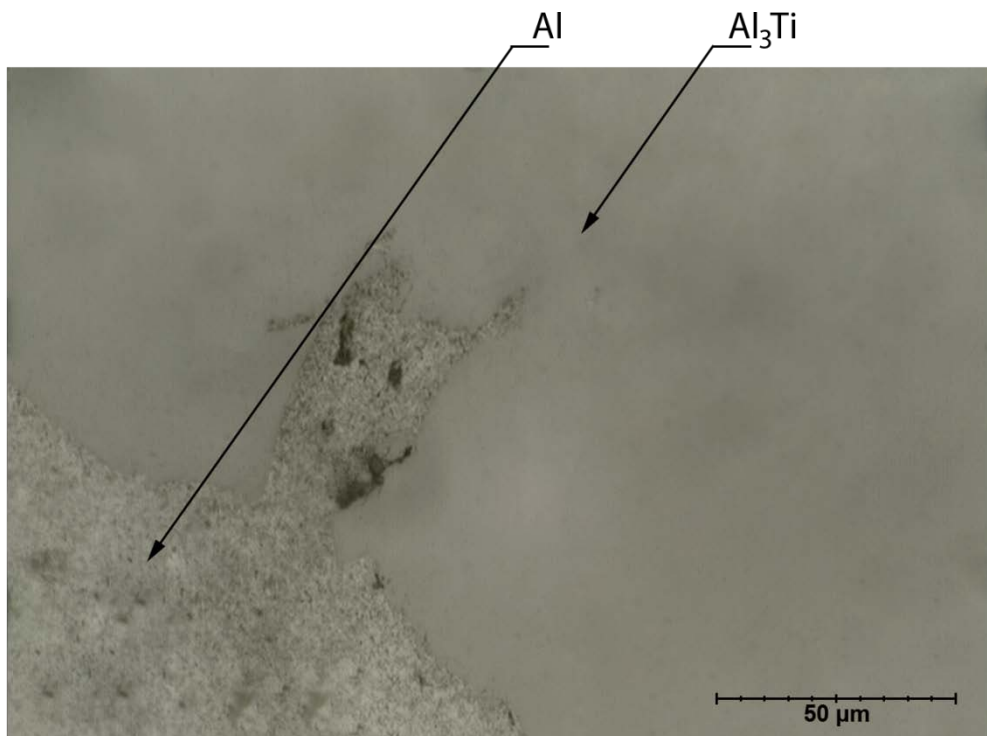


*Figure 40: Microstructure for titanium aluminide – 80 wt% Al.*

## Chapter 5: Discussions

The elongated crystals in all the microstructures are composed of  $\text{TiAl}_3$  (I) similar to the microstructures of Braun and Ellner as shown in Figures 9 and 10. The grainy region viewed in the microstructures is believed to be aluminum as it bears resemblance to Figure 1 from Yang et al.

The grainy texture is also assumed to be a porous matrix attributed to the dehydrogenation of  $\text{TiH}_2$ . In the processing of aluminum foam, small quantities of  $\text{TiH}_2$  (<1 wt%) are used and dehydrogenation is controlled to effectively generate pores. In this experiment 21-32 wt%  $\text{TiH}_2$  (20-30 wt% Ti) is loaded with the samples. Because the wire and the hydride are not packed, the end result is an arrangement of very fine pores as most of the gas escapes before the aluminum is able to melt over the  $\text{TiH}_2$  powder. Ti-70 wt% Al has a highly textured grain that can be associated with the higher  $\text{TiH}_2$  content. Ti-73 wt% Al also has a textured surface, but it is less visible than Ti-70 wt% Al. In the case for Ti-78 wt% Al, the void can be associated due to an unusual buildup of hydrogen inside the crucible.

The surface oxidation is believed to be attributed to trapped air inside the 250 mL crucible during stacking of the spacer alumina crucibles. Also, only the three crucibles arranged on the top layer displayed this visible oxidation. Figure 41 shows the Ti-Al-O stability diagram at 1123K, the operating temperature of the first chromel furnace. The first oxide to form is  $\text{Al}_2\text{O}_3$  at a  $P_{\text{O}_2}$  of  $10^{-41}$  atm; TiO and  $\text{Al}_2\text{O}_3$  coexist above  $10^{-39}$  atm. Figure 42 shows the Ti-Al-O stability diagram at 973K, the operating temperature of the second chromel furnace. The formation of  $\text{Al}_2\text{O}_3$  occurs at a  $P_{\text{O}_2}$  of  $10^{-49}$  atm and TiO above a  $P_{\text{O}_2}$  of  $10^{-47}$  atm. The stability diagram of Ti-Al-O at the vertical tube furnace operating temperature of 1873K can be seen in Figure 43.  $\text{Al}_2\text{O}_3$  makes its first appearance at a  $P_{\text{O}_2}$  of  $10^{-20}$  atm and the TiO and  $\text{Al}_2\text{O}_3$

equilibrium is at  $10^{-19}$  atm.  $\text{Al}_3\text{Ti}$  is stable at a  $\text{P}_{\text{O}_2}$  less than  $10^{-19.6}$  atm and develops into  $\text{TiAl}$  at greater  $\text{P}_{\text{O}_2}$ . The argon originally flowing into the system contains a  $\text{P}_{\text{O}_2}$  of  $10^{-5}$  atm, sufficient  $\text{O}_2$  to create  $\text{Al}_2\text{O}_3$  and  $\text{TiO}_2$ . The absence of  $\text{TiO}$ ,  $\text{TiAl}$ , and  $\text{Al}_2\text{O}_3$  in the XRD profiles is proof that the  $\text{P}_{\text{O}_2}$  of the system is below  $10^{-19}$  atm.

To create a hydride, it is crucial to decrease the  $P_{O_2}$  of the system as much as possible. Evidence can be seen in the Ti-H-O stability diagram shown in Figure 44. By decreasing the  $P_{O_2}$  of the system, a lower  $P_{H_2}$  is required to equilibrate  $TiH_2$ . The same concept can be analogous to the Al-O-H system; therefore, by reducing the  $P_{O_2}$  in an Al-O-H system, a lower  $P_{H_2}$  was needed to form aluminates (e.g.,  $AlH_3$ ,  $Al_4H_6$ ).

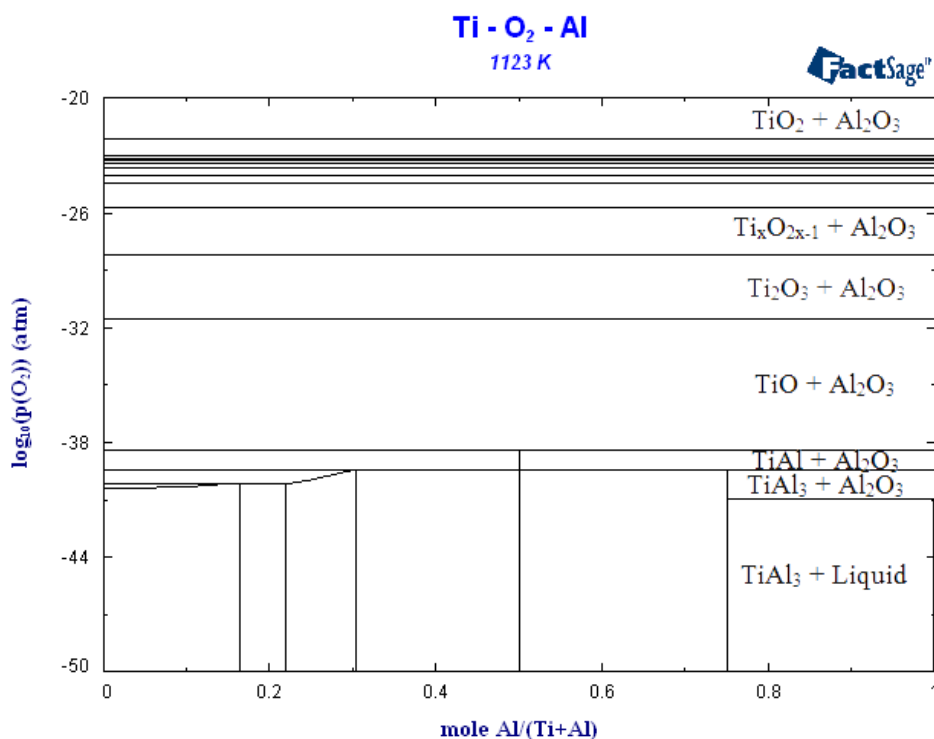


Figure 41: Ti-Al-O<sub>2</sub> stability diagram calculated by FactSage at 1123K.

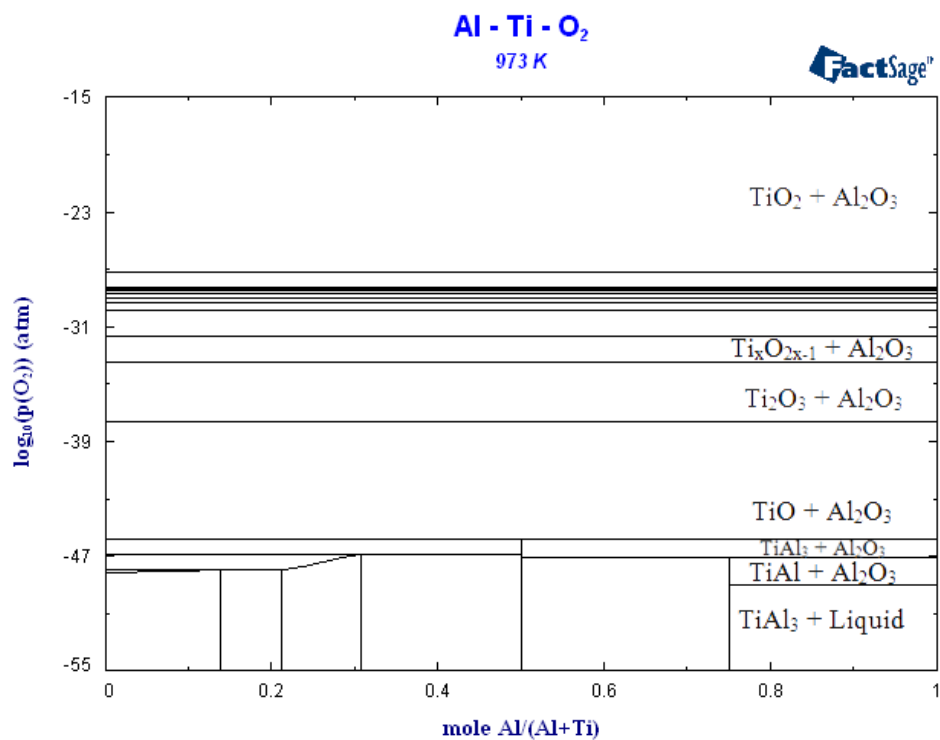


Figure 42: Ti-Al-O<sub>2</sub> stability diagram calculated by FactSage at 973K.

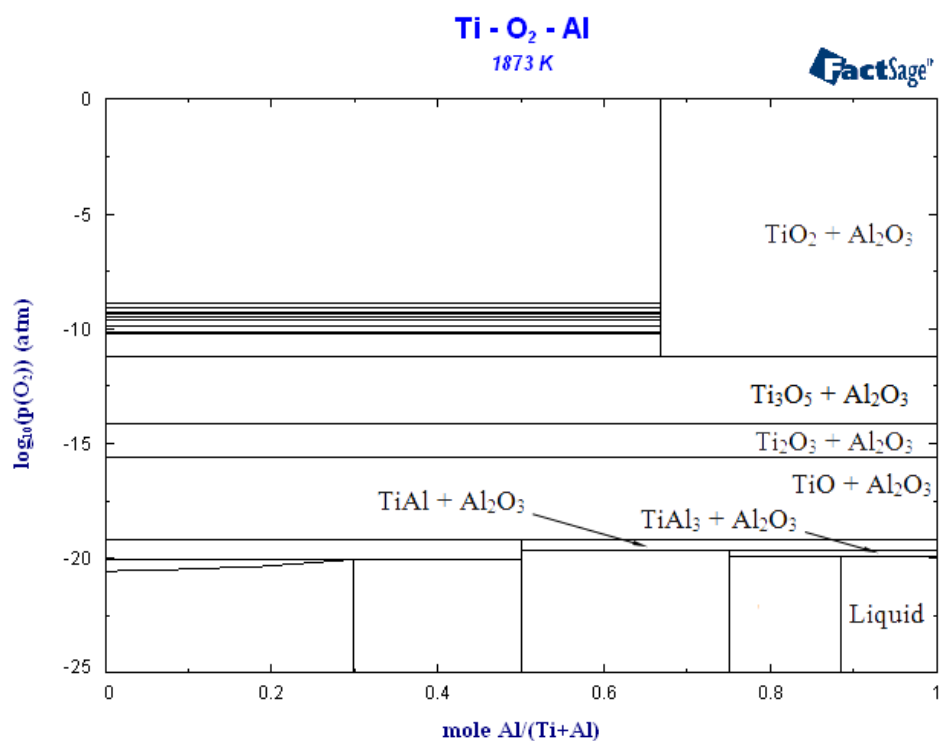


Figure 43: Ti-Al-O<sub>2</sub> stability diagram calculated by FactSage at 1873K.

# Ti-H-O, 1873 K

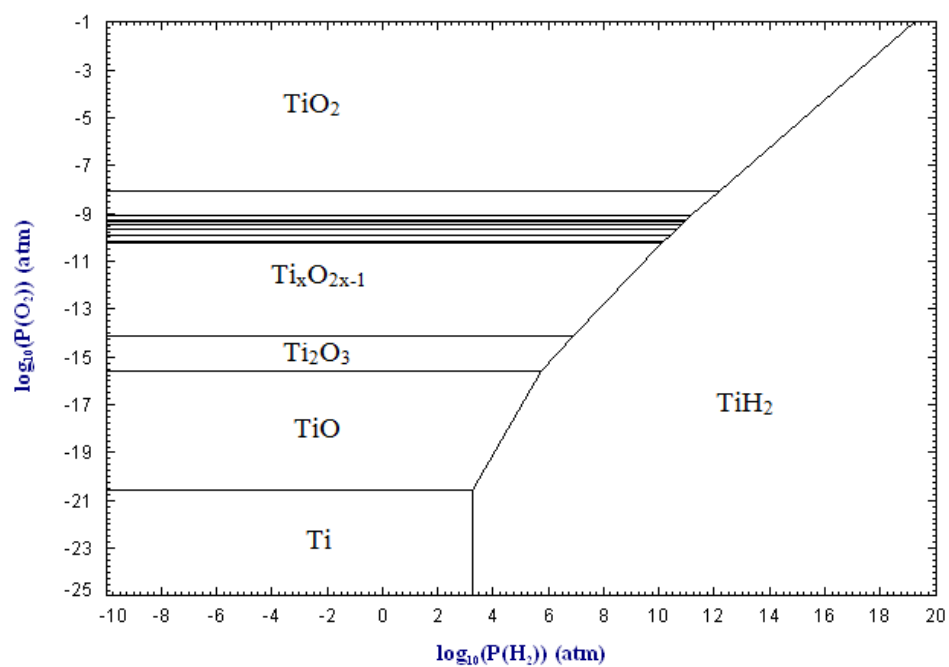


Figure 44: Ti-H-O stability diagram calculated by FactSage at 1873K.

## Chapter 6: Conclusion

The microstructures for 70-80wt% Al in titanium were investigated by melting Al wire and  $\text{TiH}_2$  in a crucible at  $1600^\circ\text{C}$  for 4 hours. The resulting samples were analyzed using an optical microscope and x-ray diffraction. All the peaks displayed contents of Al,  $\text{Al}_3\text{Ti}$  and Ti. The microstructures all display elongated crystals of  $\text{Al}_3\text{Ti}$  (l) surrounded by Al. It is deduced that the Al has partially reacted with the released hydrogen from the  $\text{TiH}_2$  powder and created very fine pores throughout the structure.

Oxygen contamination was avoided as there are signs of neither aluminum oxide nor titanium oxides in the XRD profiles. The calculated phase diagram indicated that oxygen potentials less than  $10^{-19}$  atm was achieved at 1873K because of the lack of  $\text{Al}_2\text{O}_3$  formation within the microstructure.

## References

1. Banhart, J. "Manufacture, characterisation and application of cellular metals and metal foams." Progress in Materials Science (2001): 559-632.
2. Bazyn, T., et al. "Combustion characteristics of aluminum hydride at elevated pressure and temperature." Journal of Propulsion and Power (2004): 427-31.
3. Bhosle, V., et al. "Dehydrogenation of  $\text{TiH}_2$ ." Materials and Engineering (2003): 190-99.
4. Bogdanovic, Borislac, et al. "Metal-doped sodium aluminium hydrides as potential new hydrogen storage materials." Journal of Alloys and Compounds (2000): 36-58.
5. Braun, J. and M. Ellner. "Phase Equilibria Investigations on the Aluminum-Rich Part of the Binary System Ti-Al." Metallurgical and Materials Transactions A (2001): 1037-47.
6. Duarte, I. and J. Banhart. "A study of aluminium foam fabrication - kinetics and microstructure." Acta Materialia (2000): 2349-62.
7. Gaskell, David R. Introduction to Metallurgical Thermodynamics. Washington: Hemisphere Publishing Corporation, 1981.
8. Graetz, Jason and James J. Reilly. "Kinetically stabilized hydrogen storage materials." Scripta Materialia (2007): 835-39.
9. Hashi, K., et al. "Hydrogen absorption and desorption in the binary Ti-Al system." Journal of Alloys and Compounds (2002): 547-550.
10. Heerden, D. Van, D. Josell and D. Shechtman. "The formation of F.C.C. titanium in titanium-aluminum multilayers." Acta Metallurgica (1996): 297-306.
11. Jensen, Craig M., et al. "Complex Hydrides for Hydrogen Storage." Chemical Reviews (2007): 4111-32.
12. Kitazono, K., E. Sato and K. Kuribayashi. "Novel manufacturing process of closed-cell

- aluminum foam by accumulative roll-bonding." Scripta Materialia (2004): 495-98.
13. Königsberger, E., G. Eriksson and W.A. Oates. "Optimisation of the thermodynamic properties of the Ti-H and Zr-H systems." Journal of Alloys and Compounds (2000): 148-52.
14. Li, X., et al. "Unexpected Stability of  $\text{Al}_4\text{H}_6$ : A Borane Analog?" Science (2007): 356-58.
15. Liu, H., et al. "Kinetic study on nonisothermal dehydrogenation of  $\text{TiH}_2$  powders." International Journal of Hydrogen Energy (2009): 1-8.
16. Maeland, A.J., et al. "The structures of hydride phases in the  $\text{Ti}_3\text{Al}/\text{H}$  system." International Journal of Hydrogen Energy (1999): 163-68.
17. Orimo, Shin-ichi, et al. "Complex Hydrides for Hydrogen Storage." Chemical Review (2007): 4111-32.
18. Qiu, Caian, et al. "Thermodynamic Modeling of the Na-Al-Ti-H system and Ti dissolution in sodium alanates." Computer Coupling of Phase Diagrams and Thermochemistry (2008): 624-36.
19. San-Martin, A. and F.D. Manchester. "The H-Ti (Hydrogen-Titanium) System." Bulletin of Alloy Phase Diagrams (1987): 30-42.
20. Sun, Dalin, et al. "Rehydrogenation and cycling studies of dehydrogenated  $\text{NaAlH}_4$ ." Journal of Alloys and Compounds (2004): 265-69.
21. Wang, Wei-E. "Thermodynamic evaluation of the titanium-hydrogen system." Journal of Alloys and Compounds (1996): 6-12.
22. Witusiewicz, V.T., et al. "The Al-B-Nb-Ti system III. Thermodynamic re-evaluation of the constituent binary system Al-Ti." Journal of Alloys and Compounds (2008): 64-77.



23. Yang, D.H., et al. "Effect of decomposition properties of titanium hydride on the foaming process and pore structures of Al alloy melt foam." Materials Science and Engineering A (2007): 415-26.
24. Youn, S.W. and C.G. Kang. "Fabrication of Foamable Precursors by Powder Compression and Induction Heating Process." Metallurgical and Materials Transactions B (2004): 769-76.
25. Zhang, D.L. and D.Y. Ying. "Formation of fcc titanium during heating high energy ball milled Al-Ti powders." Materials Letters (2002): 329-33.
26. Zhang, F., et al. "A thermodynamic description of the Ti-Al system." Intermetallics (1997): 471-82.

## **Curriculum Vita**

David Pham was born on April 5, 1985 in El Paso, TX. He is the third and youngest son of Tong Duy Pham and Ana Maria Pham. He obtained his Bachelor of Science in Mechanical Engineering degree at the University of Texas at El Paso (UTEP) in 2008. Shortly after, he pursued his graduate studies at UTEP for his Master of Science in Mechanical Engineering and graduated in the 2010.

Permanent address: 8645 North Loop Dr.  
El Paso, TX, 79907

This thesis was typed by David Pham.